SANDIA REPORT
SAND2012-0481
Unlimited Release
Printed January 2012

Hierarchical Electrode Architectures for Electrical Energy Storage & Conversion

Kevin R. Zavadil, Nancy A. Missert, John. A. Shelnutt, and Frank B. van Swol

Prepared by
Sandia National Laboratories
Albuquerque, New Mexico 87185 and Livermore, California 94550

Sandia National Laboratories is a multi-program laboratory managed and operated by Sandia Corporation, a wholly owned subsidiary of Lockheed Martin Corporation, for the U.S. Department of Energy's National Nuclear Security Administration under contract DE-AC04-94AL85000.

Issued by Sandia National Laboratories, operated for the United States Department of Energy by Sandia Corporation.

Available to DOE and DOE contractors from

U.S. Department of Energy
Office of Scientific and Technical Information
P.O. Box 62
Oak Ridge, TN 37831

Telephone: (865) 576-8401
Facsimile: (865) 576-5728
E-Mail: reports@adonis.osti.gov
Online ordering: http://www.osti.gov/bridge

Available to the public from

U.S. Department of Commerce
National Technical Information Service
5285 Port Royal Rd.
Springfield, VA 22161

Telephone: (800) 553-6847
Facsimile: (703) 605-6900
E-Mail: orders@ntis.fedworld.gov
Online order: http://www.ntis.gov/help/ordermethods.asp?loc=7-4-0#online

SAND2012-0481
Unlimited Release
Printed January 2012

Hierarchical Electrode Architectures for Electrical Energy Storage & Conversion

K.R. Zavadil, Sandia National Laboratories, Materials Reliability Department, Albuquerque, NM 87185

N.A. Missert, Sandia National Laboratories, Nanomaterials Sciences, Albuquerque, NM 87185

J.A. Shelnutt, Sandia National Laboratories, Ceramic Processing & Inorganics Materials, Albuquerque, NM 87185

F.B. van Swol, Sandia National Laboratories, Computational Materials Science & Engineering, Albuquerque, NM 87185

Abstract

The integration and stability of electrocatalytic nanostructures, which represent one level of porosity in a hierarchical structural scheme when combined with a three-dimensional support scaffold, has been studied using a combination of synthetic processes, characterization techniques, and computational methods. Dendritic platinum nanostructures have been covalently linked to common electrode surfaces using a newly developed chemical route; a chemical route equally applicable to a range of metals, oxides, and semiconductive materials. Characterization of the resulting bound nanostructure system confirms successful binding, while electrochemistry and microscopy demonstrate the viability of these electroactive particles. Scanning tunneling microscopy has been used to image and validate the short-term stability of several electrode-bound platinum dendritic sheet structures toward Oswald ripening. Kinetic Monte Carlo methods have been applied to develop an understanding of the stability of the basic nano-scale porous platinum sheets as they transform from an initial dendrite to hole containing sheets. Alternate synthetic strategies were pursued to grow dendritic platinum structures directly onto subunits (graphitic particles) of the electrode scaffold. A two-step photocatalytic seeding process proved successful at generating desirable nano-scale porous structures. Growth in-place is an alternate strategy to the covalent linking of the electrocatalytic nanostructures.

Contents

1.0 Introduction

Hierarchical electrodes are one enabling technology necessary to produce revolutionary improvements in the performance characteristics of electrochemical devices capable of storing electrical charge (i.e., ultra- or redox capacitors) or interconverting electrical charge and chemical energy (i.e., batteries and reversible fuel cells).[1] The multi-scale porosity of a hierarchical scaffold ensures maximum contact between electroactive phase and the electrolyte resulting in better utilization of the capacity and the resulting optimization of energy density coupled with increased mass transport and optimized power density. One strategy for creating hierarchical electrodes is to embed a nanostructured electroactive phase, with its own intrinsic nanoscale porosity, into a porous current collector that contains several successive larger length scales of porosity to serve as an electron conductive scaffold. Dendritic platinum nanostructures[2] were selected as a candidate material for this study to serve as an electroactive catalyst suitable for the reduction of oxygen as a cathodic reaction during electrochemical cell discharge (e.g., polymer electrolyte fuel cells, air batteries). Nanotextured metals are susceptible to electrochemically driven Oswald ripening resulting in particle restructuring and decreased activity over time[3]; the nanoscale porosity is lost due to electrochemical coarsening.[4,5] Evidence exists that nanostructured particles can be stabilized toward the through electrolyte (dissolution) and surface diffusion processes responsible for driving ripening.[2] The work described herein represents an attempt at better understanding the origins of ripening resistance through a joint computational and experimental effort. Activities are also focused on developing methods for anchoring platinum nanostructures to electrode surfaces to preserve both the structure and activity of these particles. New synthetic methods are developed for growing dendritic platinum structures directly on the building blocks for conductive electrode scaffolds.

2. Electroactive Nanoparticle Linking to Electrode Surfaces

2.1 Diazonium-based Binding of Pt Nanoparticles on HOPG

Specialty synthesis methods for producing electroactive nanostructures often preclude the direct integration of these structures into a hierarchical electrode scaffold. Post-synthesis assembly is routinely used in the form of liquid suspensions to impregnate or cast nanostructures into a porous solid support or physical mixing nanostructures with support particles to create porous nanocomposites. In both of these cases, minimal control exists for where the particles eventually end up within the scaffold and the degree to which they stay in contact with the current collecting scaffold. A method for covalently binding nanostructures to the support so as to anchor while preserving electrochemical function is desirable. A method for accomplishing the tethering of nanostructures to electrode surfaces is developed based on a dual-diazonium chemistry. Diazonium reactions and molecular attachment is applicable to a wide range of electrode materials including metals, metal oxide, and semiconducting materials.[6] The overall chemistry is displayed in Figure 1 for the tethering of Pt nanoparticle to a carbon surface. Figure 1 emphasizes the tendency for a diazonium ion to extract an electron resulting in the formation of a reactive intermediate capable of binding to the electrode surface. The intermediate is favored when formed on an aromatic ring, while the use of such an aromatic tether is desirable in facilitating electron transport between the nanoparticle and the electrode. A distinction is made between spontaneous[7] and electrochemically driven[8] diazonium reactions as this reaction can be

driven under equilibrium conditions or under the influence of a tuned interfacial potential. Figure 1 highlights the goal of a minimum length spacer molecule (1 phenyl unit), but in reality, the diazonium species can react to form polyphenyl chains on a surface. Question addressed within the current work focus on whether chain length can be minimized, can particles be stably attached to an electrode using this minimal chain length, and are electrochemical properties preserved.

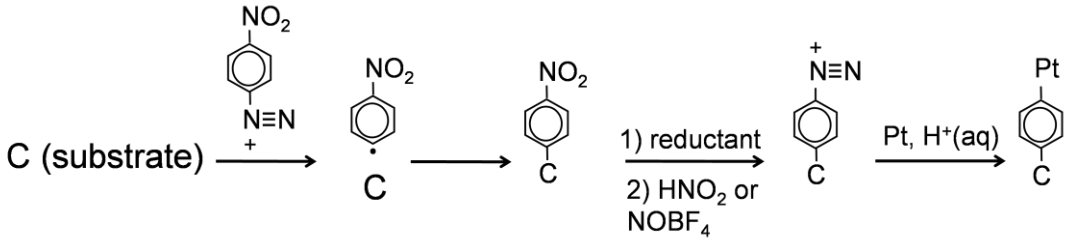

Figure 1. Schematic for a dual-diazonium chemical linking process of electroactive nanostructures (e.g., Pt nanoparticles) to conductive scaffolds (carbon).

Spontaneous deposition of the NBD species on HOPG results in aryl attachment at surface defect sites. Figures 2a,b show low force, intermittent contact AFM images (tip amplitude ~ 4 nm, f_o = 75 kHz, k = 3 N/m, under N_2) of a graphite surface incubated in 1 mM NBD:100 mM tertrabutylammonium tetrafluoroborate in acetonitrile for one hour and rinsed extensively in acetonitrile. The image shows the flat basal planes of the graphite crystal interrupted by a series of parallel step edges. Two distinct features related to the nucleation and growth of the NB film are evident in these images: 1) a 1.3 nm high topology that lines the step edges along with islands of a similar height on the open planes and 2) a distinct low density of 3 to 6 nm particles that sit on top of some of these islands. Additionally, linear chains of deposit are also seen to cross the surface planes at crystallographic angles consistent with the hexagonal symmetry of graphite. The NB layers along the step edges and the open plane islands appear to be approximately three nitrophenyl units in length (as opposed to the single phenyl unit idealized in

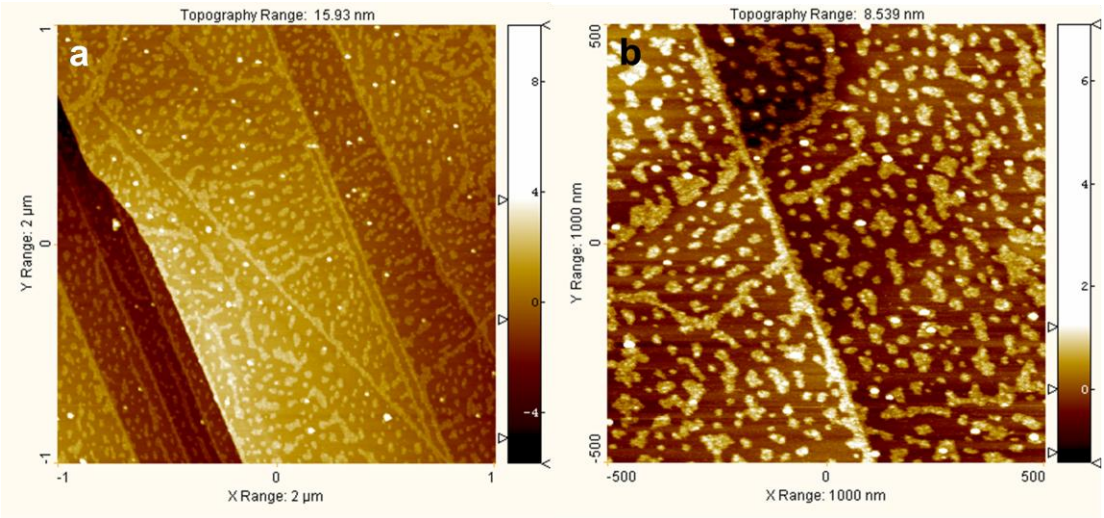

Figure 2. AFM images of spontaneously deposited nitrobenzene on HOPG showing NB attachment at surface defects.

Figure 1) based on previous STM imaging of mercaptopyridine on Au that showed that this heterocyclic ring extended 0.4 nm above the surface. The fact that spontaneous deposition occurs along step edges is consistent with the idea of radical attack at the most active surface sites. The extended linear chains on the open planes could be the result of NB attachment at mechanically strained regions of the surface. The HOPG crystals used in this study consistently exhibit large superstructures in STM imaging related to electronic perturbation produced by in- and out-of-plane translation of graphene sheets with respect to the underlying crystal. The low density of larger particles appears to result from extended growth of vertical polymeric structures that contains 2 to 5 times as many nitrophenyl units as the basic islands. These structures are seen in cathodically deposited NB films and their persistence with sonication in acetonitrile argues against being physisorbed material or remnant supporting electrolyte.

Electrochemical deposition of NB on HOPG produces a more homogeneous deposit. Figure 3a shows comparable AFM images (identical imaging conditions) for a 6 second, -800 mV (vs. Ag/Ag^{+}(nitrate):acetonitrile) deposition from the same electrolyte used to generate the data of Figure 2. Cathodic polarization leads to crystallographic planes that are covered with a nearly continuous 1.3 nm high film, with remnant void area so as to allow a height measurement. Particles of extended polynitrophenyl growth are also visible at comparable areal densities as seen for the spontaneous case. Clearly, overcoming the activation energy (overpotential) for the generation of the nitrophenyl radical leads to more homogeneous nucleation and growth. The growth is still localized as evidenced by the nodular texture of the NB island surfaces and the distribution of the void regions in the film, indicating that polyphenyl chain elongation remains a substantial competing path relative to surface attachment.

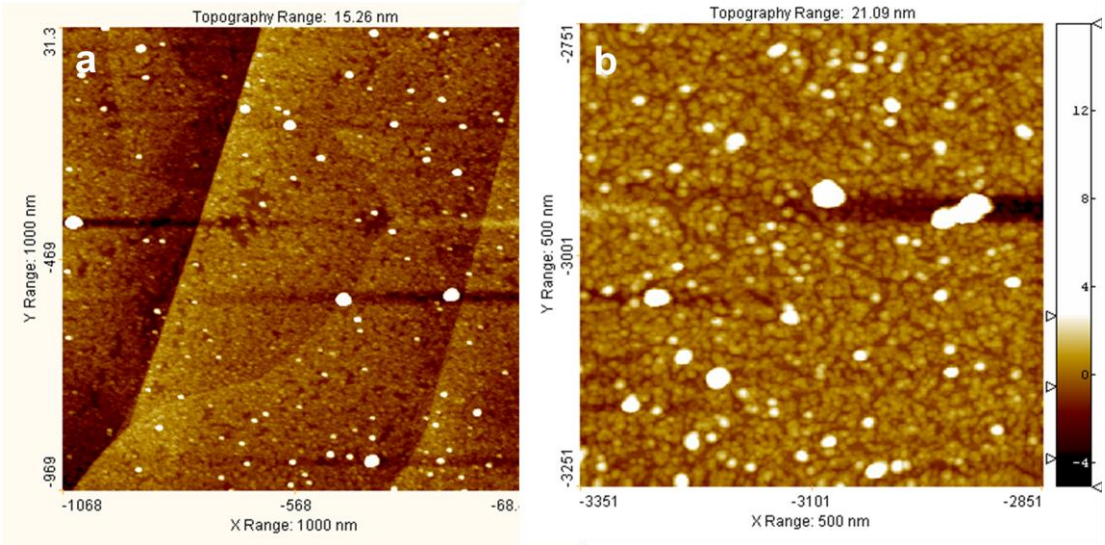

Figure 3. AFM images of a 6 and 60 second cathodic deposition of nitrobenzene on HOPG showing more homogeneous deposition with increased overpotential.

Longer periods of cathodic deposition of the film serve to infill void regions on the basal plane of HOPG and presumably increase polyphenyl chain length. Figure 3b show the background morphology of a NB film deposited at -800 mV for 60 seconds using the same electrolyte as previously described. The film structure is more compact, despite still exhibiting a nodular short range structure, with the void areas filled in. The particles representing extended growth of

nitrophenyl chains appear at higher densities and the size distribution has increased to 2 to 18 nm above the surface plane. The implication is these feature continuously nucleate through the deposition process, becoming a more dominant fraction of the surface. A more continuous NB film might be electrochemically grown at lower diazonium salt concentrations where limited mass transport discourages concentrated growth at the most active sites.

Metallic nanostructures can be chemically bonded to this polyphenyl film using the diazonium chemistry shown in Figure 1. A two-step chemical conversion of the nitro moiety to form a diazonium group serves as the active agent for substrate-metal bonding. Figure 4 shows an AFM image of a one hour spontaneously formed NB layer that was modified with a diazo moiety and exposed to a solution of approximately 4 nm diameter citrate-capped Pt nanoparticles in 100 mM H_2SO_4 for an additional one hour period. The Pt nanoparticles (brighter objects in the image) appear exclusively associated with the original NB islands with the inter-island regions devoid of particles; an expected result for the direct bonding between the phenyl rings and the Pt particles. The particles also appear to be arrayed around the perimeter of the polyphenyl islands with several instances of particles sitting on top of these islands. Particle heights above the basal plane of HOPG are measured at 4 nm with particles extending only 2.8 nm above the polyphenyl islands. The impression is that particles are either attached at island sides or are pulled down into the island interior, possibly as a result of reacting with multiple in-plane (multiple polyphenyl chains) and out-of-plane (along a polyphenyl chain) binding sites.

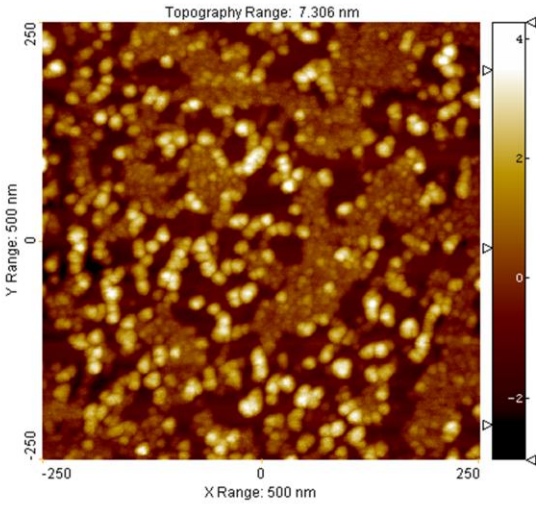

Figure 4. AFM image showing the result of attaching 4 nm Pt nanoparticles to a diazotized, spontaneously deposited polynitrophenyl film.

Spectroscopic characterization of bound particles provides more insight into the interaction between the polyphenyl linker and the particles. Near edge x-ray adsorption fine structure (NEXAFS) analysis was performed on 2 nm diameter nanoparticles linked to a Si(111) surface. Si was chosen to eliminate resonance features from an underlying carbon (graphite) electrode so that signatures from the aromatic linker were more apparent. Additionally, the (111) oriented surface of Si was chosen to favor an upright (perpendicular with respect to the surface) orientation of the biphenyl linker with Si-C bond formation. Spontaneous deposition of the linker molecule results in a nearly continuous film comprised of islands of the linker where average island height is nominally average 1.5 nm. These results indicate that a similar triphenyl species is formed as was observed in the case of graphite. Pt nanoparticles were attached to the diazotized linker modified surface resulting in a dense layer of particles, as seen for the case of 4 nm Pt in Figure 5b. Such prepared samples were analyzed as a function using NEXAFS on beamline U7a at NSLS (Brookhaven).

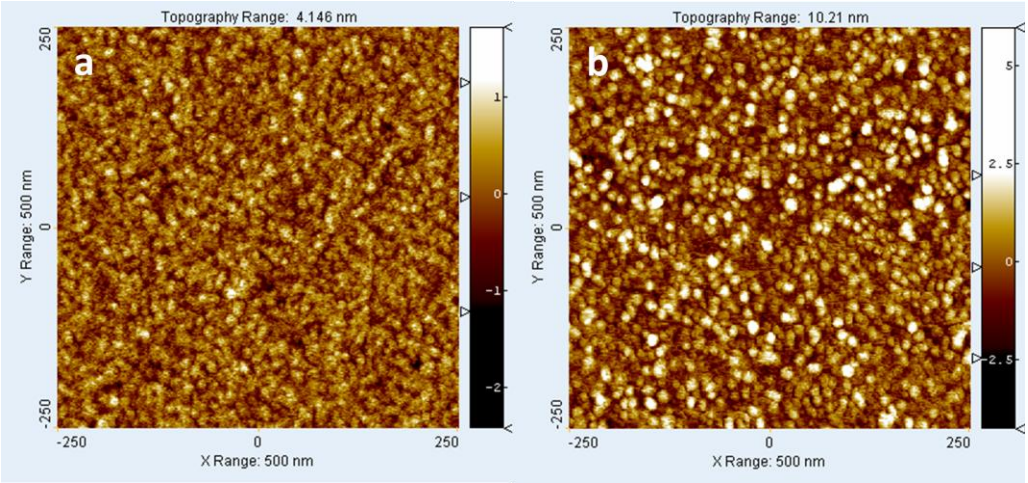

Figure 5. AFM images of the linker spontaneously reacted on a Si(111) surface (a) and after chemically binding 4 nm diameter Pt nanoparticles to the surface.

Polarized x-rays allowed the linker molecule orientation to be explored by varying the incident angle of the x-rays. Resonance spectra were acquired near the C and N K-edges in a partial electron yield mode. Example C K-edge spectra are shown in Figure 6a,b for the diazotized surface without and with the attached 2 nm Pt nanoparticles. The electron yield intensity has been linearly normalized, but individual spectra are offset vertically to facilitate comparisons. The spectra are comprised of two discrete π* resonances at 285 and 288.6 eV, along with two σ* resonance peaks at 291 and 300 eV. The π* resonances are derived from the π-bonded aromatic rings of the linker, while σ* features originate from C-H bonding states.[9] The π* resonances are of particular interest because the orientation of the individual phenyl rings with respect to the polarization vector of the incoming x-ray will dictate the relative intensity of these peaks. For the experimental configuration used, an in-plane phenyl ring (parallel to the Si surface) will create enhanced π* emission at a grazing angle (20°), whereas σ* intensity will be enhanced at normal incident angle (90°). The spectra in Figure 6a,b show that in the presence of bound Pt particles

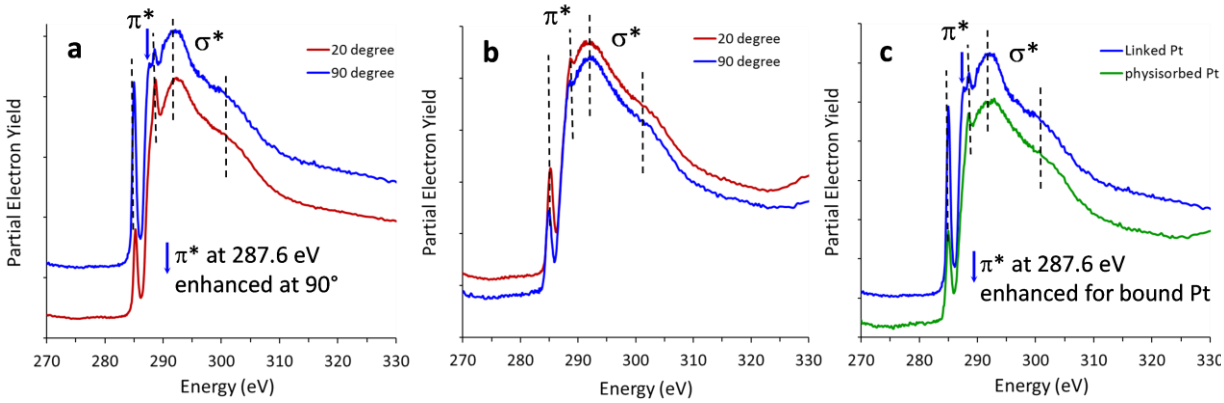

Figure 6. C K-shell excitation spectra for (**a**) Pt bound to the triphenyl linker and (**b**) the linker without Pt at grazing and normal incidence using p-polarized x-rays. Spectra from the linker with bound Pt and unbound (physisorbed) Pt at normal incidence (**c**).

the π* resonances are enhanced at normal incidence arguing that a greater fraction of total phenyl groups are bound perpendicularly to the surface. However, in the absence of Pt a small but measureable π* enhancement exists at a grazing versus normal angle. Clearly, some fraction of the triphenyl linker has re-oriented with the binding of Pt and has rotated from a planar to a vertical orientation. Noteworthy is the fact that an apparent minor shoulder at 287.6 eV on the higher energy π* resonance is enhanced when Pt is bound to the linker. The presence of this feature appears related to some combination of Pt-C bound formation and phenyl-phenyl bond rotation, as Pt particle physisorbed onto the non-diazotized linker film does show this enhancement (Fig. 6c).

The origin of linker reconfiguration is related to the reactive binding of the Pt nanoparticle. Results for particles bound to triphenyl linker on HOPG showed that the particle is pulled down into the linker film with reactive binding. This partial immersion of the particle would be expected to create compressive stress in the linker film possibly sufficiently large enough to drive phenyl-phenyl group rotation to accommodate the particle, as depicted for a simple biphenyl linker in the schematic of Figure 7. A vertical orientation of this phenyl ring would be expected to better electronically couple the two resonance systems together resulting in more efficient (lower barrier) electron transport to and from the tethered particles facilitating electrochemistry at the nanoparticle

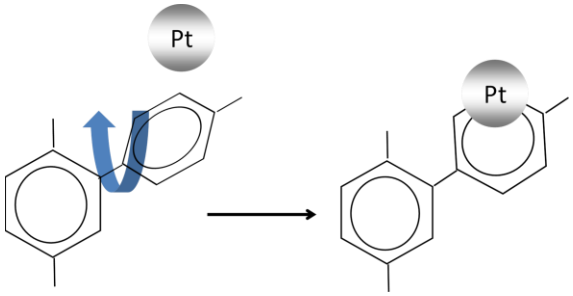

Figure 7. Hypothesized biphenyl linker reconfiguration induced by the submergence of a Pt nanoparticle into the linker film. Bond rotation produces an increased number of vertically oriented phenyl rings yielding π* resonance enhancement in NEXAFS.

2.2 Demonstration of Preservation of Nanostructure Electroactivity

Chemical binding between the linker and attached nanostructures can be inferred by exploring the electrochemical activity of the attached nanostructure. Figure 8 shows the results of cycling the potential of glassy carbon electrodes prepared with either diazo-bound (chemisorbed) and physisorbed 4 nm Pt nanoparticles in an acid electrolyte in the presence (saturated) and absence of dissolved O_2. For chemically bound nanoparticles at O_2 saturation, the current response is dominated by the O_2 reduction reaction with an onset of reaction at 380 mV (vs. Ag/AgCl) and a diffusion dictated maximum at ca. 60 mV. Physisorbed Pt nanoparticles also show a response toward O_2, however, the onset of reaction does not occur until a potential well below 300 mV and current is reduced relative to the bound particle case, never reaching a diffusion limiting condition at potentials above 0 mV. The voltammetry observed in the absence of O_2 for bound particles exhibits the surface oxidation of Pt on the anodic sweep at mV, the reduction of the

surface in the peak at mV, and the reductive adsorption of H and evolution of H. These voltammetric attributes for the physisorbed case are consistent with larger overpotentials and kinetic limits toward electron transfer from electrode to unbound particles. Simple particle contact with the linker layer is not sufficient for facile electron transport that is provided when the nanoparticle is bound to the linker layer. The delocalization of electron density for the polyphenyl linker and the phenyl-Pt bond should produce a low barrier for electron transport. Lower physisorbed particles density can be ruled out as a possible cause of the lower current because AFM images show comparable surface particle densities for the bound and unbound cases. We note that larger roughness parameters are measured in images of the unbound particles indicating that the particles are not submerged into the linker layer, consistent with the NEXAFS results discussed previously.

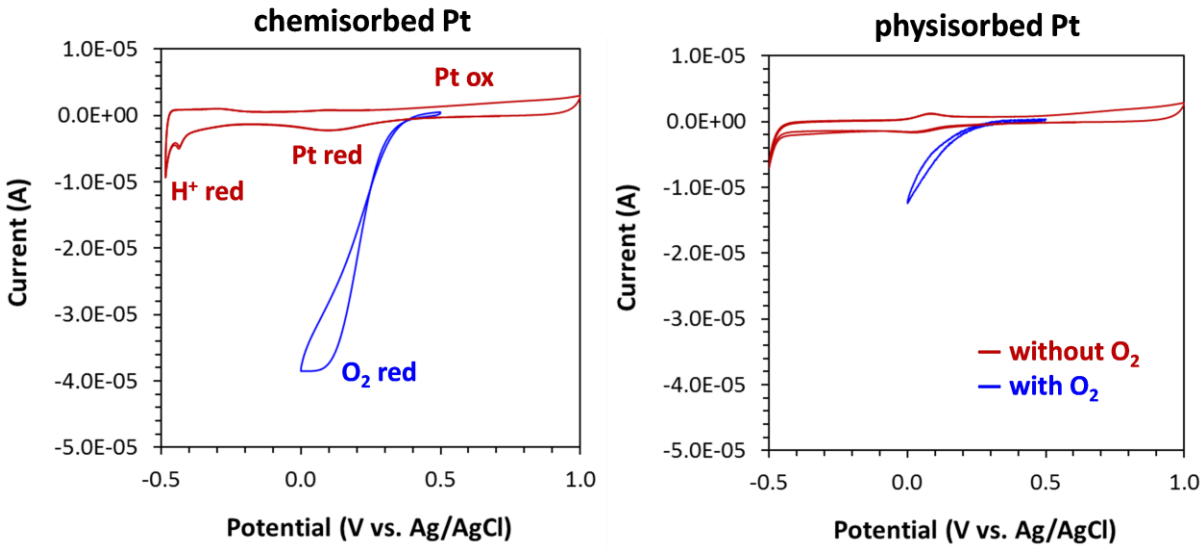

Figure 8. Comparison of cycle voltammetric response for chemically bound (chemisorbed) and unbound (physisorbed) 4 nm diameter Pt nanoparticles on a polyphenyl film on glassy carbon (100 mM H_2SO_4) in the presence and absence of O_2. Specific oxidation (ox) and reduction (red) reactions are indicated.

The diazo-bonding scheme works well for larger nanostructures. Figure 9 shows the results of chemically binding dendritic nm thick Pt nanosheets to the basal plane of graphite. The larger sized, two-dimensional character of these structures, as seen in the SEM image of Figure 9a, require some degree of control of the orientation of the sheet with respect to electrode surface if the goal is to place the sheet flat against the electrode. Sedimentation and sheet carrier solvent drying were used to first place the sheet in contact with the graphite surface followed by the development of capillary forces between the sheet and the surface to pull the structure against the surface. The center sheet seen in the SEM image of Figure 9b demonstrates that it is possible to orient structures parallel to the electrode using this approach. Flat structures become more easily addressable using scanning probe microscopy, as seen in the AFM image displayed in Figure 9b, to better explore their durability as they function in an electrochemical environment. Chemical binding of the sheets are again inferred from their electrochemical response, as shown in Figure 9c. A sedimented sheet population bound to a glassy carbon electrode using the dual diazonium

linking chemistry yields a clear response for oxygen reduction when comparing voltammetry in air equilibrated and de-aerated dilute sulfuric acid. These results suggest that some degree of covalent bonding per sheet has occurred and that larger nanostructures can be attached to electrode surfaces using such linking schemes.

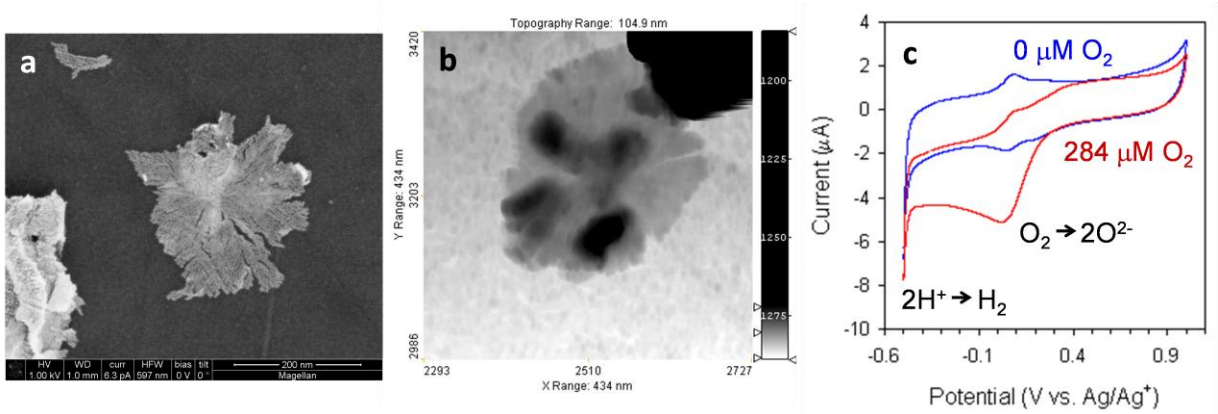

Figure 9. SEM (a) and AFM (b) images of dendritic Pt nanosheets chemically linked to the basal plane of graphite. Resulting voltammetric response toward O_2 in 100 mM H_2SO_4 – 284 μM for air and 0 μM for N_2 equilibration.

3. Experimentally Derived Stability of Pt Dendritic Structures

One of the goals of this project was to use scanning tunneling microscopy to determine whether nanoscale ripening processes resulting from electrochemical cycling could be observed experimentally in order to validate models and mechanisms. Two types of systems with nanostructure on different length scales were investigated: Pt foams (Fig. 10a) and sheets (Fig. 10b).

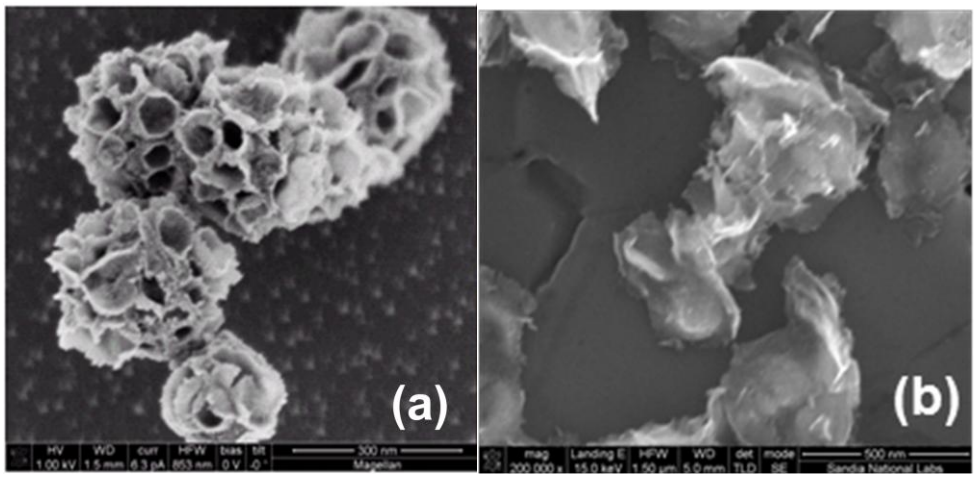

Figure 10. (a) SEM image of Pt foams (b) SEM image of Pt sheets.

Flame annealed Au was chosen as a substrate because it provided inert, atomically flat terraces. Initial experiments were performed in air to assess tunneling characteristics and ultimate resolution. Considerable effort was undertaken to obtain layers with a high distribution of single

foam cluster and small clusters of sheets that allowed stable tunneling. Sedimentation layers deposited directly on the Au surface resulted in large clusters or mobile foams. Application of a 2-aminoethanethiol layer to the Au surface (Fig. 11a) allowed tethering of the foams (Fig. 11b) and sheets along with stable tunneling in both air and 0.1M H_2SO_4.

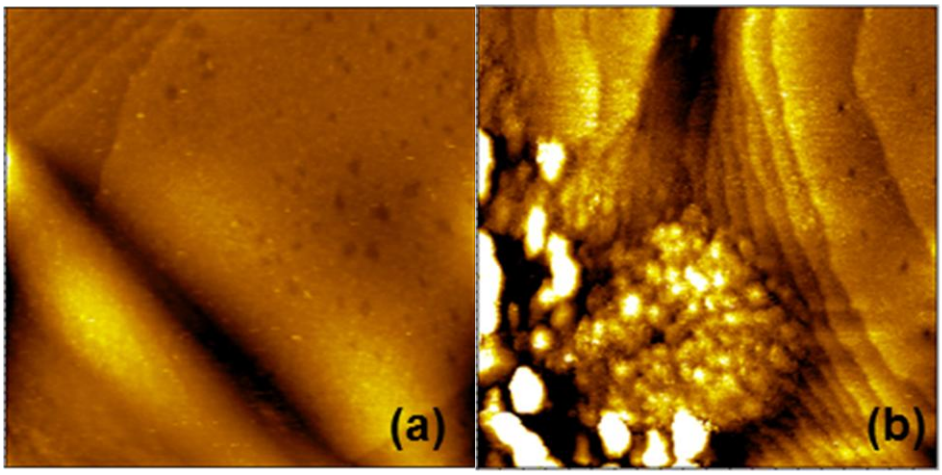

Figure 11 (a) STM image of 2-aminoethanethiol layer on Au terraces (b) STM image of a single Pt foam tethered by 2-aminoethanethiol to Au terraces. Both images are 1x1 µm.

The Pt foams on Au substrates were cycled between 0.05 – 1.2 V (vs SHE) in 0.1M H_2SO_4 (Fig. 12a) and imaged by STM before cycling (Fig. 12b) and following 10, and 100 cycles, (Fig. 12c). No change in the surface morphology was detectable. Before and after cycling, the foam morphology was dominated by a 3 – 50 nm nodule structure.

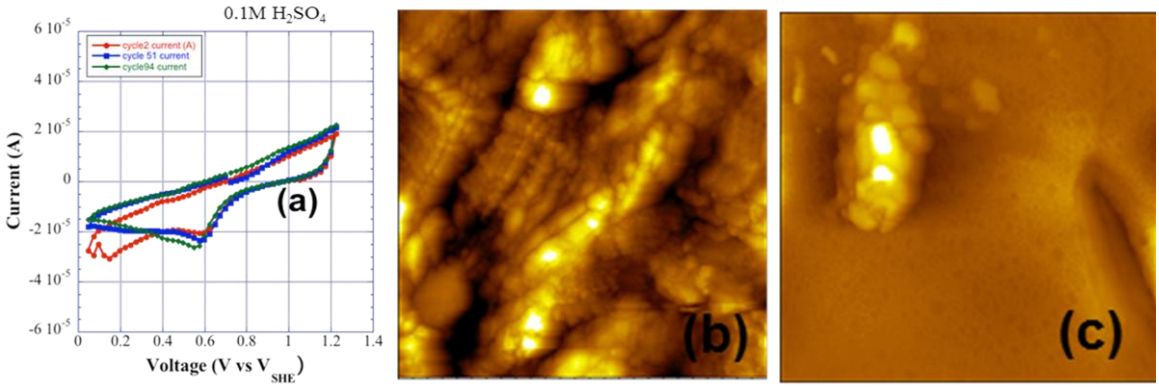

Figure 12. (**a**) Current- voltage characteristic during potential cycling of Pt foams in 0.1M H_2SO_4. (**b**) STM image of large foam morphology prior to potential cycling. 500 x 500 nm image. (**c**) STM image of small foam following 100 potential cycles. 500 x 500 nm image.

The stability of the nanostructure on Pt sheets was also investigated as a function of potential cycling, (Figure 13a). Although the 2-aminothiol layer on Au provided tethering capability for the sheets, we were unable to obtain a high distribution of single flat sheets. Instead, the sheets tended to form small clusters, where the nanoscale surface morphology could be observed at the edges of the clusters, (Figure 13b). Here no significant change in the surface morphology was

observed following 10, 100, and 770 cycles. Before and after cycling, the sheet morphology was dominated by a 3- 10 nm nodule structure.

Although no change in surface morphology was observed down to the 3-10 nm scale, there could well be surface ripening at the atomic level. The resolution obtained here may have been limited by residual surfactants remaining from the foam and sheet fabrication. In any case, we observed that ripening of these model structures did not occur above this scale following up to 770 potential cycles in 0.1M H_2SO_4.

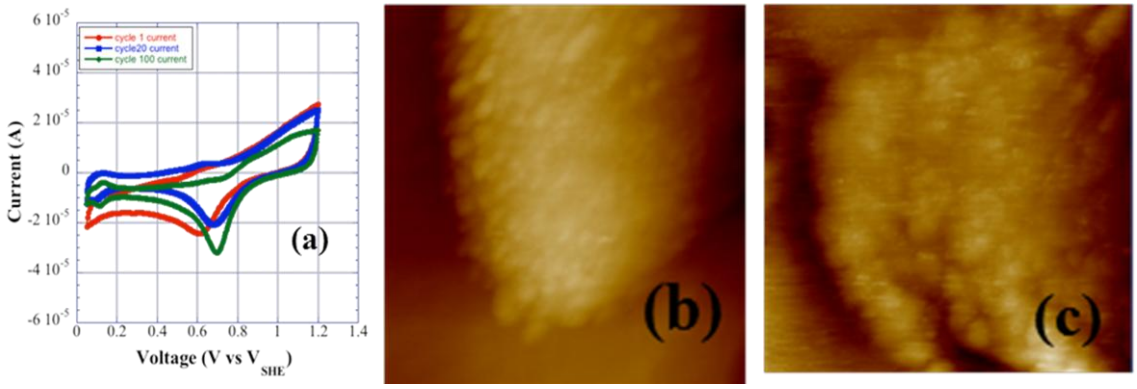

Figure 13 (a) Current- voltage characteristic during potential cycling of Pt sheets in 0.1M H_2SO_4. (b) STM image of sheet morphology prior to potential cycling. 100 x 100 nm image. (c) STM image of sheet following 770 potential cycles. 100 x 100 nm image.

4. Computational Studies of Pt Holey Sheets

4.1. A Thermodynamic Perspective of Holey Sheets: the Role of Curvature

From a thermodynamic perspective the stability of the holey sheet appears to present a problem in that such a structure combines regions of flat surface with curved surfaces. After all, it is well known that the vapor pressure of a curved particle is larger than that over a planar surface by an amount that is proportional to $2\gamma/R_c$, where γ is the surface free energy per unit area, and R_c is the radius of curvature (e.g., equal to one half of the particle radius for spherical liquid droplets). Hence, stably combining flat and curved regions would not appear possible. To resolve this issue and allow a detailed discussion of the holey sheet stability we will first summarize the more familiar curvature effects as encountered with droplets and bubbles.

The result that the curvature of a convex particle increases the vapor pressure can be demonstrated from applying the usual conditions for thermodynamic equilibrium to phase coexistence which, for a pure component, means that the temperature (T) and chemical potential (μ) is the same in both phases and, in addition, that there is mechanical equilibrium. The last condition simply amounts to equal pressures when two phases meet at a flat interface. However, if the surface is curved then there must exist a pressure difference across the interface. This result is due to Laplace who first stated that this pressure jump is equal to $2\gamma/R_c$; the pressure of the phase on the convex side being lower than that of the other. Thus, for a convex liquid (or solid) particle with a (positive) radius of curvature R_c we have the following conditions for equilibrium

$$T_1 = T_2$$
$$\mu_1 = \mu_2$$
$$p_2 - p_1 = \frac{2\gamma}{R_c}$$

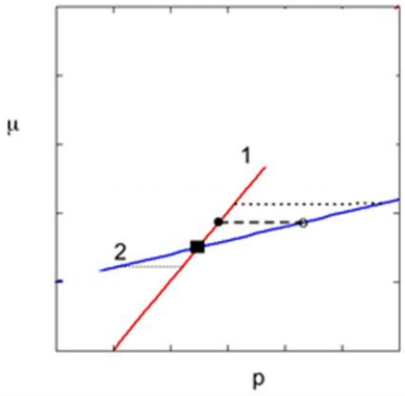

Figure 14. Chemical potential versus pressure of a pure substance

Where the subscripts 1 and 2 denote the vapor and liquid (or solid) phases respectively. These conditions specify coexistence that occurs in the presence of a non-planar interface separating the two phases. To demonstrate that the conditions expressed above lead to an increased vapor pressure for a convex particle compared to a flat particle it suffices to consider a bulk μ,p diagram (for some fixed T) for a pure substance, sketched in Figure 14. Here the steep curve corresponds to vapor phase (labeled "1") and the other ("2") to the dense (liquid or solid) phase (recall that the slope $\partial\mu/\partial p = 1/\rho$, where ρ denotes the density). The bulk phase coexistence (or saturation) point corresponds to the intersection of the two curves and is denoted by the solid square, which is denoted (p_{sat}, μ_{sat}). This unique point corresponds to phase coexistence across a planar interface, where the pressures in both phases are simply equal, i.e., $p_2 = p_1$. In contrast, the equilibrium condition for a curved particle in the μ,p plane corresponds to two *separate* points, one on each curve, denoted by a solid circle (phase 1) for the dilute phase and an open circle for the dense phase. The dashed tie-line connecting the two indicates that these two phases are at equilibrium. Notice that the pressure of phase 2 exceeds that of phase 1 (i.e., by an amount $2\gamma/R_c$, a positive quantity for a convex particle), and that both pressures exceed the bulk coexistence pressure. Notice also that the tie-line must be parallel to the horizontal axis since the two chemical potentials must equal each other. The figure demonstrates that this common chemical potential value exceeds the bulk phase coexistence value, i.e. by an amount $\Delta\mu \equiv \mu - \mu_{sat}$,.

These observations complete the proof of the statement above that the vapor pressure of a convex equilibrium droplet surrounded by vapor exceeds that of the planar case. It is worthwhile emphasizing the simple nature of the construction of the proof. Given Laplace's result for the pressure jump across a curved interface the statement follows immediately because the density of phase 2 is larger than that of phase 1. But notice that the equilibrium states involve one state point (i.e. phase 1, denoted by the solid circle) that necessarily lies on a metastable branch. This implies that we implicitly assumed that the underlying phase transition was first-order (so that a metastable branch can exist), as it is for solid and vapor, and as it is for liquid and vapor (except right at the critical point). Clearly then, the argument provided can be assumed to have most validity for large radii of curvature, which keep the system close to the bulk phase coexistence point, and hence the bulk equation of state for each individual phase is still a good approximation for that of the phases involved. There obviously must be a limit to how small a droplet one can consider as the vapor metastable branch is of finite length, ending at the spinodal.

It is easy to see how to generalize the result described above. For instance, according to Laplace a smaller droplet will have a larger pressure difference across the interface. A tie-line for a smaller particle is illustrated in the figure by a heavy dotted line in Figure 14. A larger pressure difference implies that the tie-line must move upward in the μ,p diagram, and hence the new pressures p_2 and p_1, as well as the equilibrium chemical potential must now deviate more from the bulk coexistence point (solid square).

Consider a system consisting of two droplets of different size in a common (i.e., shared) vapor. From the above it immediately follows that this situation can not represent true equilibrium, as the different sizes would require a different vapor pressure for each droplet: higher for the smaller droplet. This can not be accomplished in a common vapor. Such a situation will necessarily mean that the size of the droplets must evolve with time. Remarkably, the naïve assumption that the two droplets would move toward equal size is wrong. Such a state would indeed correspond to a local extremum in the total free energy, but it would be a local maximum and therefore unstable. Instead, the evolution must proceed in the direction of one droplet, by a process that will involve the disappearance of the smaller droplet. This, again, follows from the observation that a small droplet will have a larger vapor pressure, and hence a density gradient in the vapor phase will develop when a small and large droplet share a common vapor phase. This then must lead to net evaporation from the small droplet and net condensation onto the large droplet, moving the entire system toward one droplet, which represents a minimum in the total free energy. This process is known as Oswald ripening.

If the curvature of the meniscus is convex with respect to the dense phase 2, the radius of curvature will have a negative sign. This implies that the pressure of the dense phase is now the smaller of the two coexisting phases, i.e., $p_2<p_1$. This case is encountered with bubbles of vapor inside a liquid (or solid), and a familiar demonstration of historical importance that clearly demonstrates and quantifies the pressure difference is the phenomenon of capillary rise of water in a small glass tube. From the discussion above, it quickly follows that equilibrium across a convex interface implies a tie-line that lies *below* the bulk coexistence point. This case is indicated by the light dotted line in Figure 1. Notice that this time it is the higher density phase that is metastable, and that both pressures and the chemical potential are smaller than at the bulk-coexistence point (solid square).

Ostwald ripening described for two droplets can also occur for two bubbles in a common dense phase, a liquid say. Just as in the droplet case, the evolution will be in the direction of the larger bubble growing at the expense of the smaller one, resulting in a final state of a single bubble with a radius of curvature that is larger than either one of the two bubbles.

The arguments for Ostwald ripening, applied to two curved objects in material contact through a common phase, can be equally well employed to the case of a solid particle that exhibits a nonuniform curvature. For instance, consider a solid particle with the structure of a peanut shell that is nonconvex, and has regions of both positive and negative curvature. Just on the basis of curvature such a particle should evolve into a convex spheroidal particle. The Ostwald ripening mechanism described earlier (i.e., vaporization from large positive curvature regions and condensation onto regions of negative curvature or small positive curvature) can again be used. However, that does not imply that vaporization/condensation or transport through the vapor

phase is the dominant or even relevant mechanism. Instead, a surface diffusion may well be the relevant mechanism, especially when the vapor pressure is low. This illustrates, inter alia, that the process of Ostwald ripening is less about the details of molecular transport than about direction of lowest free energy. We point out that different regions of curvature on a *fluid* particle would, of course, be much more likely to evened out by fluid flow than by diffusion.

We are now in a position to assess the situation of the stability of a holey nano-sheet. The surprise at this point is that a curved region (the hole) is in apparent stable equilibrium with the flat regions that comprise the sheet. Numerous observations of nano-particles indicate that such particles exhibit rapid sintering, and Ostwald ripening. Indeed, our experiments show this: the early evolution of the Pt dendrite into a Pt holey sheet is driven by a reduction of curvature. Thus, we can expect that the kinetics of surface diffusion and/or evaporation/condensation is sufficiently rapid to produce coarsening. This then points at the existence of a thermodynamic explanation: it indicates an absent or a small driving force. In other words, the holey sheet must represent a local, and hence stable, minimum in the free energy. The only possibility for such an explanation is to be found in the curvature. The flat surface has, of course, zero curvature, i.e., $R_c = ¥$. Therefore, stability of the hole points at near zero-curvature of the surface of the hole.

Obviously, one of the principal radii of curvature, R_x say, of a hole of circular cross section is negative with a magnitude approximately equal to that of the hole radius. That would imply that other principal radius curvature R_y (which is in a direction orthogonal to R_x), is of equal magnitude but opposite sign. This type of surface is known as a catenoid, see Figure 15a, a surface of revolution for which Euler showed that it has an internal (and thus also external) surface that is exactly of mean zero curvature (a "minimal" surface). It is, in fact, the only surface of revolution, other than a plane, that has that property. The catenoid has a radius that varies with height *z* as *cosh(z/c)*, where *c* is a positive constant. The catenoid surface is very

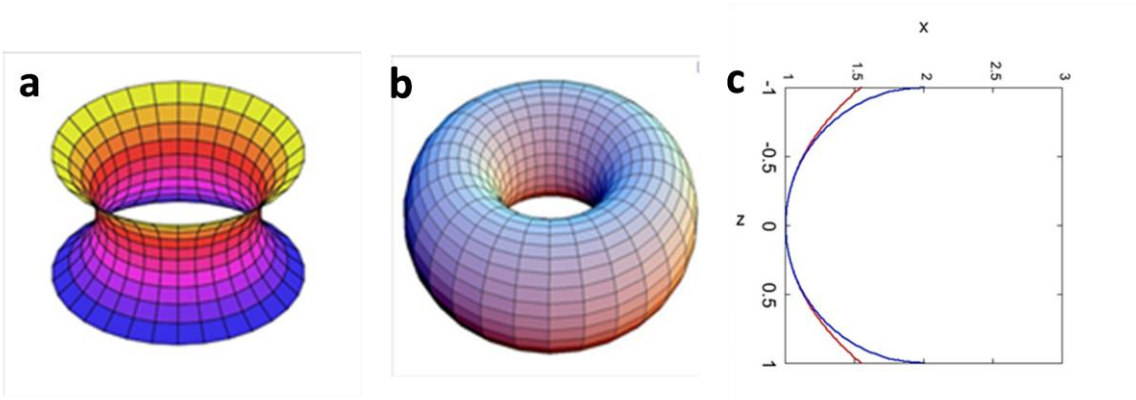

Figure 15. Catenoid (a) and torus (b) shapes and a comparison of their surface shapes (c) - catenoid (red) and torus (blue)

similar to the classic shape of a torus (cf., donut hole, Fig. 15b) that has the radius of the hole equal to the radius of the tube (see Figure 15). This is illustrated in more detail in Figure 15c, where we compare the surface shape of a catenoid (a hyperbolic cosine; red curve) with that of a torus (a circle; blue curve). Here *z* is the direction along the symmetry axis of the hole, i.e., perpendicular to the sheet. From this comparison we conclude that we can use the circle as an

excellent approximation of the inner surface shape. The approximation is at its worse at the top and bottom of the hole. However, that is also the region where the hole-surface meets the top and bottom planar surfaces of the sheet. The catenoid meets the planar surfaces in a discontinuous manner, which leads to a free energy penalty. The circular shape on the other hand provides a smooth merging; continuous and sharing the tangent, indicating that the actual surface would fall somewhere in between the two.

We are now in a position to estimate the size of a stable hole in a sheet of thickness *h*. Given our observation that a stable hole must have a surface with zero mean curvature it follows (using the circle approximation) that the diameter of a stable hole would be equal to *h*. Holes with diameters smaller than *h* have a negative mean curvature, and would be expected to evolve by filling in. Holes with diameters exceeding *h* would have positive mean curvature, and would hence be expected to continue to grow in diameter.

The prediction above can be compared with the experimentally obtained nanostructures as well as with model structures. Starting with the experimental system, holey Pt metal nanosheets, these nanostructures exhibit stable holes which have diameters that are very similar to the sheet thickness. The lattice gas model simulations led to structures very similar to the Pt structures and hence are in agreement with the thermodynamic prediction. However, given that the Pt structures formed with essentially one thickness the test of the thermodynamic prediction can not be considered comprehensive. The lattice gas model, on the other hand, provides a straightforward and convenient vehicle to perform a systematic test. Thus, we generated various model sheets of thicknesses ranging from h = 2 to 19 atoms thick, in which we made holes with diameters ranging from 1 to 12. Simulations were then run for each case, and the evolution of the hole was determined to be stable, or otherwise growing or closing. This stability analysis showed that stable holes are those holes that possess a diameter similar to *h*. A complete stability map is shown in Figure 16. The region of stable structures appears to broaden as the absolute dimensions (i.e., thickness and hole diameter) increase.

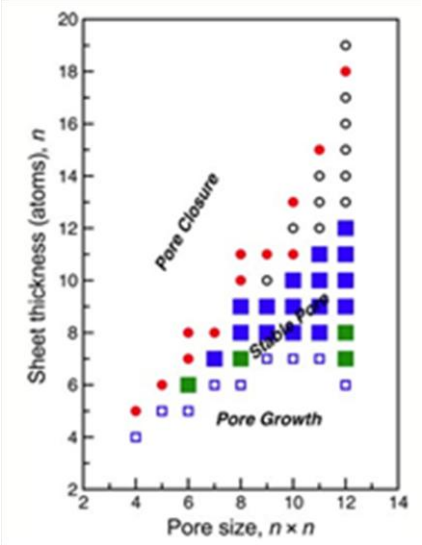

Figure 16. Stability map showing the relationship between stable hole diameter and sheet thickness.

4.2 Curvature Effects: the Melting Temperature of Nanoparticles

As discussed above, curvature affects the thermodynamic properties. A pronounced effect, for small particles, is the observed decrease in the melting temperature, inversely proportional to size. This is known as the Gibbs-Thomson effect. We have performed a molecular dynamics (MD) study of this effect for Pt particles, using the embedded atom potential. Various particle shapes and sizes were considered, namely: Mackay icosahedron (an example is shown in Figure 17. A regular polydehron with 20 identical equilateral triangular faces) which is a platonic solid (that is not spacefilling) and consists of tightly packed shells of particles leading a 'magic'

number of atoms (i.e., 13,55,147,309,561,923,1415,2057 corresponding to a total number of 1 through 8); regular decahedron, Ino decahedron and a Marks decahedron.

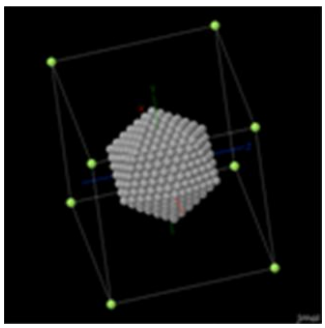

Figure 17. Mackay icosahedron

An example is shown in Figure 18a, where we show the melting curve of three different sized Mackay icosahedra (each cluster labeled by the magic number of atoms, corresponding to 3,4 and 6 shells). We plot the potential energy versus temperature. In each case the melting curve displays straight-line behavior until a fairly sharp melting transition takes place and the particle becomes a liquid drop. The height of the jump reflects the latent heat accompanying the first order melting transition. The vertical placement of the curves reflects the fact that the smaller the particles the larger surface energy contribution to the energy per particle. In each case the particles underwent surface and shape reconstruction (to a spheroidal particle shape) prior to the actual melting transition, vertices and edges becoming more rounded. A weak signature is seen in the melting curves: a slight upward bending of the curve just prior to melting. The melting point depression, $\Delta T=T-T_{sat}$, can be understood and analyzed with the help of Figure 14, relating the depression (i.e., deviation from bulk coexistence) to the size (i.e. effective radius, R). The macroscopic analysis based on Laplace's equation predicts a 1/R dependence. Expressing R in terms of the cube root of the number of particles, i.e. $N^{1/3}$ is common (see Pawlow), and this is shown in Figure 18b, which confirms a linear relationship between ΔT and $N^{1/3}$, and thus supporting the basic tenet of curvature dependence.

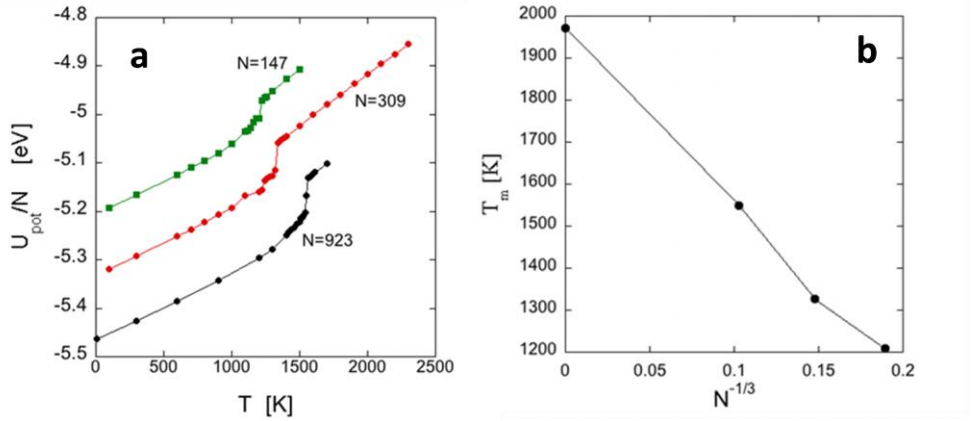

Figure 18. The melting curves for three of icosahedra particle sizes (a) and the Laplace derived variation in particle melting temperature with size (b).

4.3 Interfacial Effects: Surface Melting Temperature of Planar Interfaces

The surface reconstruction that was observed prior to melting of the crystallites can be viewed as as surface melting, a surface phase transition whereby a thin liquid layer is produced, intruding between the bulk crystal and the bulk vapor. At the surface melting transition the free energy of prematurely converting a number of crystal layers into liquid is balanced by the reduction in total surface free energy that results from replacing the single crystal-vapor interface by two

interfaces: crystal-liquid and liquid-vapor. Surface melting can (but does not have to) occur for certain solids and specific crystallographic directions. We studied the behavior of the three most close-packed surfaces of fcc Pt : the (111), (110) and (100) surfaces, by generating a thick slab of an fcc crystal.

In each case the temperature was increased in small steps, while the lateral (and periodic) dimensions were expanded according to the volume expansion with temperature at zero pressure that we determined in a *bulk* study. The results are summarized in Figure 19, where we plot the potential energy per particle as a function of temperature (cf., Figure 18). The bulk curve (no surfaces) is shown for comparison. The increase of the potential energy per particle for the slabs is entirely due to the surface energy contribution. We note that the surface free energy of the (100) and (110) surfaces is indistinguishable, but noticeably larger than the (111) surface energy. A precise determination shows that the difference is about 1 eV/nm^2.

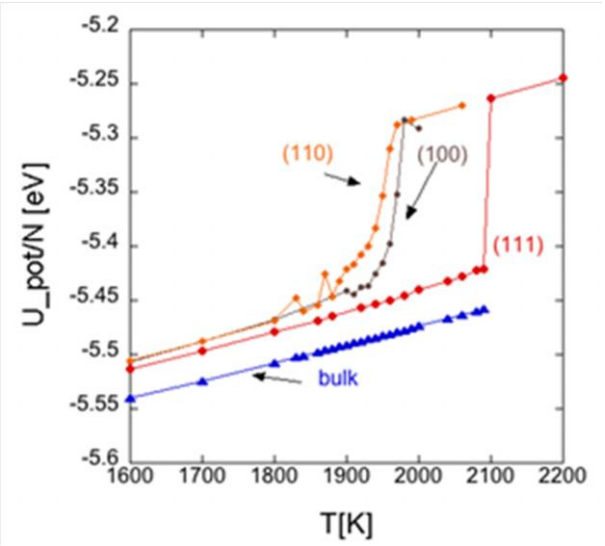

Figure 19. Surface melting curves for the three low energy orientations of Pt versus that of the bulk.

Consider the curve for a crystal slab with two (100) surfaces. As the temperature reaches about 1900 K the potential energy starts to climb to about -5.398 eV per particle. At this point the system has surface-melted 4-5 layers on each side of the slab. The density profiles perpendicular to the interface are shown in Figure 20. Here, for clarity, we show only the interfacial region of the profile on the left hand side of the slab. The center of the slab is roughly at $z/\sigma = 18$, and the other interface is located at approximately $z/\sigma = 30$ (here σ is an accurate measure of the diameter of a Pt atom). Over a range of approximately 20K (which corresponds to about 1 % of the melting temperature) we see that first the ~2-4 outer layers start to merge and exchange

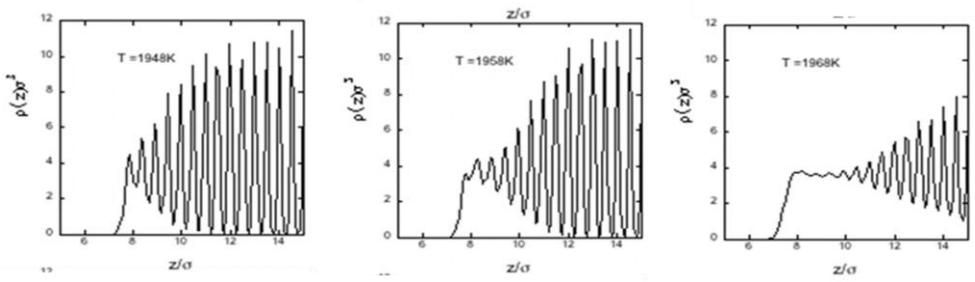

Figure 20. Variation in density with distance into the surface of a (100) Pt slab at indicated temperatures.

atoms (as evidenced by a non-zero local density between peaks), and these become liquid (bottom panel) as the temperature is increased. The thin liquid film is an equilibrium state: the

center of the slab remains crystalline while the surface consists of a thin fluid layer. As the temperature is increased the thickness of the fluid layers grows. Finally, at about 1977K, the entire slab has become fluid. The last stage of that process is expected to depend on the thickness of the entire slab, and in fact constitutes a form of *capillary* melting. The latter occurs when the free energy of the remaining crystal region in the middle of the slab can no longer be balanced by the surface free energy cost of maintaining two closely spaced crystal-fluid interfaces. At that point, the free energy of the entire system will be lowered upon melting the remaining crystal, even though the crystal in a bulk system would still be stable. That also indicates that the completion of the melting of the entire film (roughly between T = 1968K and 1978K) takes place slightly below the bulk melting temperature for this model. The surface melting phenomenon for the (110) surface is very similar, but starts at a temperature that is about 20-30K below the surface melting temperature of the (100) surface. The completion of melting appears to coincide with that of the (100) slab.

In contrast, the (111) surface, which is the most densely (i.e. hexagonally) packed, does *not* exhibit any indications of surface melting, either in the potential energy or the density profiles. Instead, the *entire* crystalline film becomes unstable all at once, around 2100K. One expects, since melting in 3D is a first-order transition, that there is some degree of hysteresis with the melting of the (111) crystalline slab, and hence 2100K likely represents an upper bound for the bulk melting temperature.

Comparing the melting of Pt nano-clusters and the melting of Pt surfaces we note that the crystallites melting temperatures fall far below (by several hundreds of K) that of surface melting on the planar (100) and (110) interfaces. This, indirectly, demonstrated that for a holey sheet we can expect substantial rearrangement to occur at temperatures (around 1500K), which is well below the surface melting temperature.

4.4 Molecular Dynamics Simulations of Pt Holey Sheets

To supplement the lattice gas studies we performed MD simulations of a finite Pt sheet from which we removed a number of atoms to create a roughly cylindrical hole. Figure 21a shows a starting configuration where the top surface is a (100) surface, while Figure 21b shows same structure at a later time following equilibration at 600K (Note: due to the periodic boundaries the 'separate' piece on the left of the frame is in fact connected to the rest of the structure through

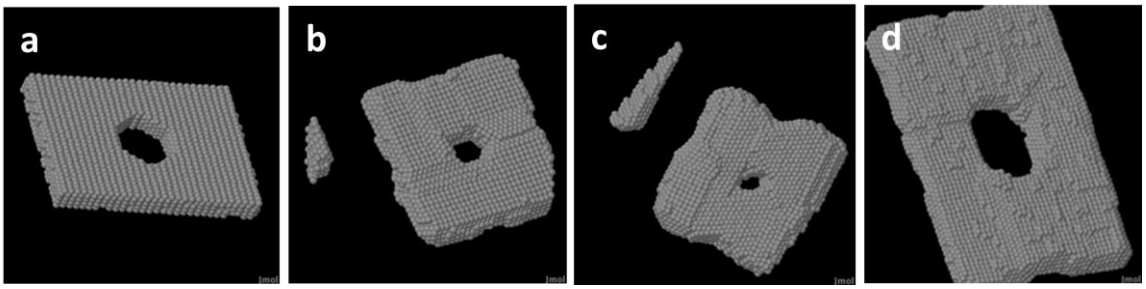

Figure 21. Results of MD simulations for oriented Pt slabs with a cylindrical hole and undergoing ripening at elevated temperature: (a) initial (100) slab, (b) the (100 slab equilibrated at 600K, (c) a comparably dimensioned (111) slab equilibrated at 900K, and (d) a large scale simulation of a (100) Pt slab equilibrated at 900K.

the boundary on the right). We notice that a significant amount of restructuring has taken place, including some warping. Evidently, the initial structure contains a significant amount of stress, that is quickly relieved by slip planes and grain boundaries. In Figure 21c, we show the result of a simulation of (111) oriented Pt sheet of comparable size, thickness and hole diameter run at 900K. Here too we observe extensive restructuring and warping. In additional the hole has been reduced in effective diameter. Figure 21d shows the results of a larger simulation for a greater thickness slab with a larger hole diameter. This is a sheet with a (100) surface, and the temperature is 900K. This structure clearly shows that the surface of the hole has both positive and negative curvature.

5. Conducting Electrocatalytic Nanostructure Growth on Electrode Supports

5.1 Photocatalytic Control of the Growth of Platinum Dendrites on Carbon Supports

Nanocomposites consisting of metal nanoparticles (NPs) supported on carbon nanomaterials (CNMs) have drawn considerable attention due to various applications as components of supercapacitors,[10] gas sensors,[11] biosensors,[12-14] hydrogen storage materials,[15-16] photoelectrochemical devices,[17] and polymer electrolyte membrane (PEM) fuel cells.[18] An advantage possessed by some of these nanocomposites is the synergistic interaction and electrical connectivity between the metal NPs and the CNM. An example is the strong interaction between nickel clusters and multilayer films of C_{60}.[19] The dispersion of NPs supported on the carbon surface is also important and can be enhanced by avoiding aggregation of the NPs on the carbon surface. The latter increases the stability of the NPs[20] by avoiding some ripening processes.[21] CNM-NP composites are conventionally achieved via two general synthetic pathways. One method is to deposit and grow NPs directly onto the CNM surface and the other is to attach pre-formed NPs to the CNM through covalent bonding.[22] Direct deposition of metal salts followed by reduction is a simple and effective method, producing large amounts of metal NPs immobilized on CNM surfaces. However, this direct synthesis method does not typically give adequate control over the NP size, shape, and Pt loading, parameters that are closely related to efficient utilization of materials.[23-26] The exploration of new synthetic methods that allow improved control over the size, shape, and loading of the deposited metal NPs is key to producing advanced CNM-NP nanomaterials.

Herein we describe a new method of growing dendritic platinum nanostructures on carbon black (CB) that allows control over the size, size uniformity, and loading of Pt dendrites on carbon surfaces. We have previously demonstrated that dendritic platinum can be grown in various shapes by templating on soft molecular assemblies, including peptide tubes, surfactant micelles, bicelles, multilamellar vesicles, unilamellar liposomes, liposomal aggregates, and reverse micellar networks. Templated growth on these structures produces a wide variety of platinum nanostructures such as peptide-nanotube/nanoparticle composites,[27] globular nanodendrites,[28-29] dendritic nanowheels,[30] flat dendritic nanosheets,[28,31] foam-like nanospheres composed of convoluted dendritic sheets,[29,31] nanocages,[32] and nanowire networks,[33] respectively. Furthermore, by incorporating molecular photocatalysts into these templating molecular assemblies, the size and size uniformity of the platinum nanostructures can be delicately controlled by variation of the light exposure and the Pt complex concentration. However, because of the high visible light absorptivity of carbon nanomaterials, direct photocatalytic synthetic methods are not easily applied to CNMs.

In the present study, we have modified the synthetic methods of photocatalytic seeding and catalytic dendritic Pt growth to provide a new and versatile procedure for growing globular platinum dendrites on CB nanomaterials. To accomplish this, a separate photocatalytic seeding step[29] was developed,

which is then followed by seed deposition and catalytic dendritic growth step. This two-step procedure allows Pt mass loadings to be controlled in the range from 10 to 80 wt% by varying the initial concentration of the Pt(II) complex. Specifically, a stable monodisperse suspension of Pt nanoparticle seeds are produced photocatalytically using a Sn(IV) porphyrin photocatalyst. These seed particles are adsorbed onto the CB at the desired surface density for subsequent catalytic growth of the dendrites. Besides acting as a photocatalyst for reduction of Pt complex, the porphyrin also maintains the monodispersity of the seed nanoparticles, allowing them to be evenly deposited onto the carbon surface. After deposition, growth of seeds in a dark autocatalytic reaction with ascorbic acid as the reductant produces the surface-bound globular Pt dendrites. These globular Pt dendrites are found to conform to the shape of the nanoscale carbon materials as they grow, providing strong interaction with the carbon surface. This two-step synthetic method is light-controlled, simple, fast, and environmentally benign. It produces uniform dendritic platinum nanostructures with tunable sizes and loadings that have potential applications as nanoscale catalysts and electrocatalysts and other possible uses.

5.2 Methods for Photocatalytically Controlled Growth

Potassium tetrachloroplatinate(II) (K_2PtCl_4; 99.99%) and L-ascorbic acid (99+%) were of the highest purity available and used as received from Sigma-Aldrich (St. Louis, MO). Electro-conductive CB (800 m^2/g) was obtained from Ketjen Black International Company Ltd. (Tokyo, Japan). Water-soluble tin(IV) porphyrins were purchased from Frontier Scientific Inc. (Logan, UT). Sn(IV) meso-tetrakis(sulfonato-4-phenyl) porphyrins (SnTPPS4), Sn(IV) meso-tetrakis(N-methyl-4-pyridyl) porphyrin (SnTNMePyP), Sn(IV) protoporphyrin IX (SnProtoP), Sn(IV) uroporphyrin I (SnUroP), and Sn(IV) meso-tetrakis(4-carboxyphenyl) porphyrin (SnTCPP) and used without further purification. The 6 chemical structures of the porphyrin photocatalysts are shown in Figure 22. All aqueous solutions were prepared with ultrapure water from a Barnstead Nanopure water system (Chesterland, OH).

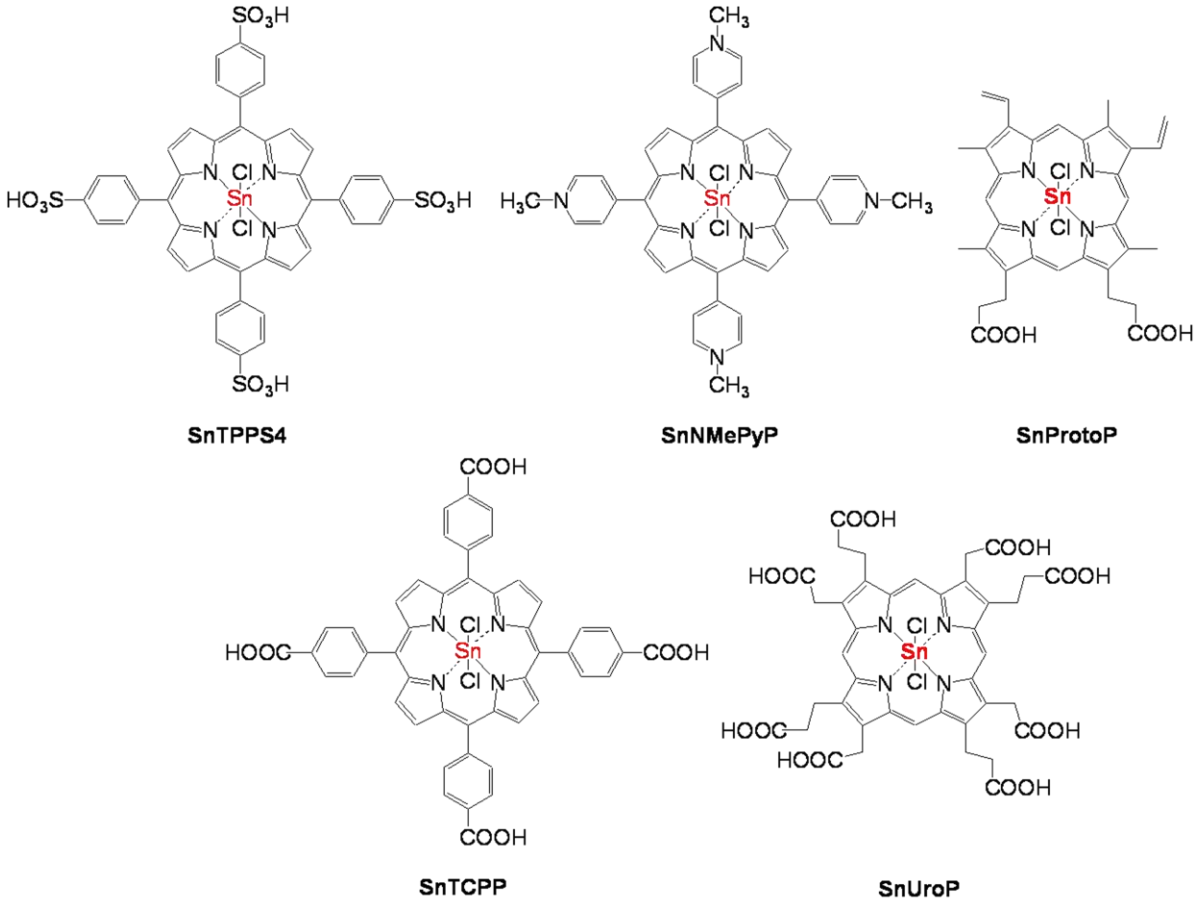

Figure 22. Structures of the Sn porphyrin photocatalysts.

Platinum(II) stock solutions were prepared by dissolving K_2PtCl_4 in water under ambient condition and aged for at least 24 h prior to being used in a synthesis. Aging the platinum solution disproportionates the complex into an equilibrium mixture of 42% $Pt(H_2O)_2Cl_2$, 53% $Pt(H_2O)Cl_3^-$, and 5% $PtCl_4^{2-}$.[34] The porphyrin solutions (30-250 μM) were prepared by dissolving the solid porphyrin powder in Nanopure water under mild sonication. The ascorbic acid solution (150 mM) was freshly prepared to avoid its gradual oxidation in air.

In a typical synthesis, an aqueous mixture (20 mL, pH 3) containing CB, Pt complex (0.28-10 mM), and ascorbic acid (75 mM) as the electron donor was prepared by stepwise addition of the above reagents to a glass reaction vessel, followed by mild sonication for 10 minutes to suspend the CB. The reaction vessel was left under ambient condition while stirring for at least one hour. When stirring was discontinued, black precipitate settles to the bottom of the reaction vessel and the supernatant was colorless and transparent. The reaction volume has been enlarged to as much as 1.6 L to produce more than 1 g of Pt/CNM nanocomposite. The amount of Pt precursor used is determined by the desired Pt mass loading in the composites (defined as the weight percentage of Pt in the Pt-CB nanomaterial).

In a representative reaction, 10 mL of 76 μM SnProtoP, 9 mL of Nanopure water, 1 mL of 20 mM K_2PtCl_4, and 0.264 g of AA were placed in a 20 mL glass vial. The mixture was stirred and

irradiated with two incandescent lamps (2 x 800 nmol-cm^{-2}-s^{-1}) for 30 minutes. The same procedure was also applied to similar reaction systems using 10 mL of 63 μM SnUroP, 71 μM SnTCPP, 100 μM SnTNMePyP, and 60-500 μM SnTPPS4.

Generally, 1 mL of the above platinum seed preparation obtained using 83 μM of SnTPPS4 and 2 mM of the platinum salt was mixed with 10 mg of CB in a 20-mL glass vial, followed by 5 minutes of mild sonication to distribute the seeds onto the carbon. Next, 10 mL of 0.15 M AA and 2.05 mL of 20 mM Pt(II) were added and the mixture was allowed to react for at least one hour under stirring. Similarly, 5 mL of the platinum seeds were used and the Pt(II) was accordingly lowered to 1.85 mL to hold a constant platinum loading on carbon (45 wt%). These syntheses were also enlarged to produce gram-scale quantities of the nanomaterials by increasing the volume of each reagent.

The black precipitates obtained from the above large-scale syntheses were collected by decanting the supernatant after centrifugation (IEC Centra®MP4R, Golden CO) at 3500 RPM. Nanopure water (200 ml) was added to the precipitates and the materials were re-suspended by simultaneous mild sonication and mechanical stirring for 15 minutes. The black slurries were transferred to four tubes and centrifuged at 3500 RPM for at least 30 minutes to precipitate the products. The supernatant was again removed. This re-suspension/centrifugation procedure was repeated for at least seven times to remove as much salts and other impurities as possible. The wet black precipitates were dried in oven for 12 h at 65ºC and used for differential thermal analysis-thermogravimetric analysis (DTA-TGA), X-ray photoelectron spectroscopy (XPS), and X-ray diffraction (XRD) studies.

Transmission electron microscopy (TEM) was accomplished using a 200-keV JEOL 2010 microscope equipped for energy-dispersive X-ray (EDX) spectroscopy. High resolution TEM (HRTEM), high-angle annular dark-field (HAADF) scanning TEM (STEM) images were obtained using a 200-keV JEOL 2010F microscope. Scanning electron microscopy (SEM) was done using a 1-30-keV Hitachi S-5200 microscope. The samples for TEM analysis were prepared by adding drops of product solutions onto standard holey carbon coated copper grids and the excess solvent was wicked away with a tissue paper. The grids were then washed several times with a drop of Nanopure water that was wicked away to remove salts and surfactant. The grids were allowed to dry in air. The samples for SEM imaging were prepared on doped silicon wafers using the same procedure as above.

A Vacuum Generators XPS system with an Al Kα X-ray source and a CLAM II electron energy analyzer was used to measure the photoemission from the purified and dried powder nanocomposites on silicon wafers. The takeoff angle, defined as the angle between the sample surface and the detector orientation, ranges from 30 to 80° at 10° increments. All spectra were taken at the base pressure of 10^{-9} Torr in an ultrahigh vacuum (UHV) XPS analysis chamber. A Shirley-type background correction was applied to the spectra. The composition of the platinum dendrites on CB was investigated by DTA/TGA using a STD 2960 Simultaneous DTA/TGA-DSC 2010 instrument with dry air as the processing atmosphere and a heating rate of 10 ºC per minute. XRD spectra were recorded on a Siemens D500 diffractometer using Ni-filtered CuKα radiation with λ = 1.5418 Å in θ-2θ scan mode using a step size of 0.05º and a 90-s step time. The samples were supported on a sheet of quartz. UV-visible (UV-visible) spectra from 180-800

nm were obtained using a HP 8452A diode array spectrophotometer (Colorado Springs, CO) and a 1-cm path length quartz cell.

5.3 Characterization of Platinum Nanodendrites on Carbon Black without Seeding

The chemical reduction of platinum complex (2.1 mM) by ascorbic acid (75 mM) in the presence of carbon black (10 mg) yielded a black precipitate. This reaction was accompanied by a color change of the supernatant from yellowish to transparent and colorless, indicating that the platinum complex is reduced and may have been deposited onto the carbon. The UV-visible spectra (Figure 23) of the mixture obtained before (red line) the reaction and also after one hour (blue) confirm that the reaction has gone to completion. Specifically, the three characteristic absorption peaks of the platinum complex appearing at 322, 384 and 472 nm disappear after one hour indicating that all Pt(II) complex has been converted to the metal.

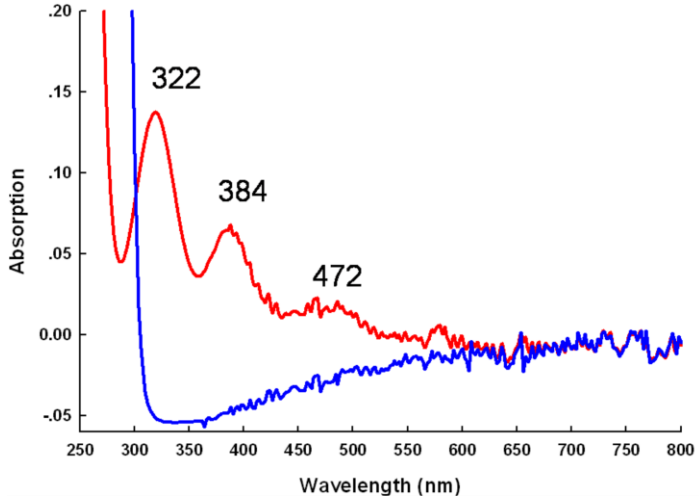

Figure 23. UV-visible spectra of a reaction mixture containing aged K_2PtCl_4 (2.1 mM) before (red) and after the one-hour of reaction time (blue).

TEM imaging of the black precipitate, which can be re-suspended in water by mild sonication, reveals an abundance of platinum nanostructures supported on CB as can be seen in Figure 24a. The nanostructures are Pt dendrites ranging from 5 to 55 nm in diameter, and they are virtually all adsorbed on carbon as the TEM images show very few Pt nanostructures not associated with the CB. This is consistent with reports[28,31,32,35-37] showing that Pt metal prefers hydrophobic environments like the CB surface. The conversion efficiency from Pt precursor to CB-supported platinum metal is near 100%, a desired feature of a synthesis using a precious metal. Interestingly, some of the Pt nanostructures have a hemispherical shape, matching well the curvature of the underlying carbon support. Many of the other dendrites likely conform to the shape of the carbon surface, but only those that are correctly oriented in the TEM images reveal the underlying CB shape.

The high-magnification micrograph in Figure 24b more clearly shows the dendritic character of the platinum nanostructures. These Pt dendrites resemble the globular Pt nanodendrites previously synthesized by our group[28,29] using a similar reaction mixture but containing surfactant micelles as templates instead of CB. The lattice fringing evident in the HRTEM micrograph of a Pt dendrite on CB in Figure 24c shows its single-crystalline nature. The small (~12 nm) globular dendrites investigated previously were found to be single crystals, but as the dendrites become larger multiple crystalline domains are to be expected. The dendrite in Figure 24c may have more than one domain, and some bending of the lattice is noticeable in this view

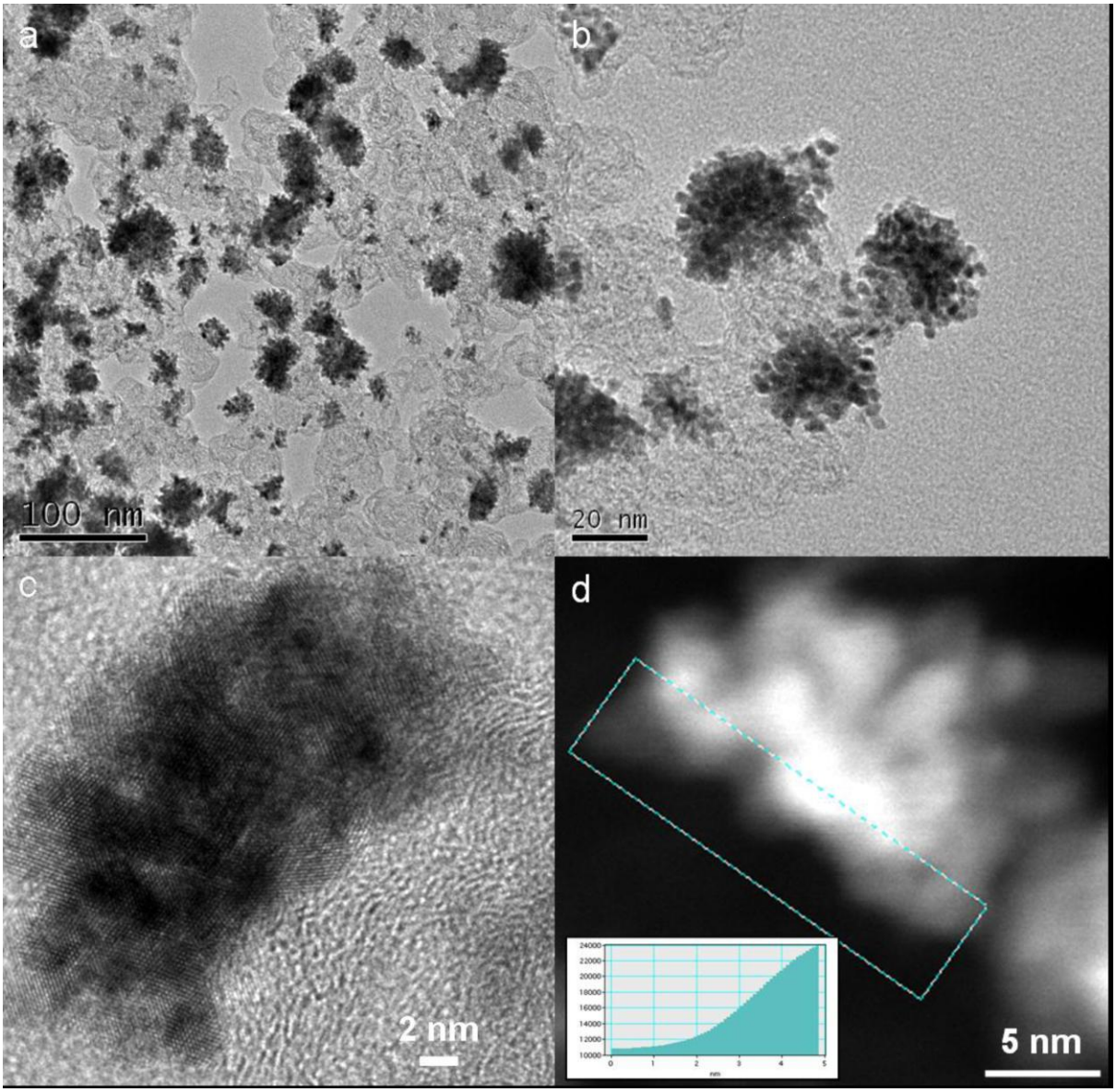

Figure 24. TEM images of platinum nanodendrites supported on CB at low (a) and high (b) magnifications, respectively. (c) A HRTEM image of a dendrite on carbon; (d): HAADF STEM image of a platinum nanodendrite. (Inset: density profile of platinum along the direction normal to the Pt/C interface in the selected area.

down the hexagonal axis. In addition, the lattice fringes are not well formed at the Pt/C interface compared to those of the bulk part of the dendrite. This could be due to the lattice mismatch

between carbon and platinum, and is suggestive of fairly strong physical adhesion of the dendrites onto carbon.

To further investigate the Pt/C interface, HAADF STEM images were also obtained (Figure 24d) to improve contrast between Pt and carbon.[38] Due to the low Z number, the carbon support is not discernable in the image while the Pt dendrite has a nearly flat edge at its contact with the carbon surface. In HAADF images, the brightness is related to the density of platinum. For the selected rectangular area at the Pt/C interface, the platinum density profile (Figure 24d, Inset) exhibits a smooth transition along the direction normal to the interface, rather than a sudden jump. Since carbon black was not chemically functionalized, bonding between non-zero valent platinum and functional groups on the carbon surface is not anticipated. We suggest that Pt atoms may have deposited into the rough carbon surface thus creating a transition region composed of both carbon and platinum, and this may explain why the Pt nanodendrites so strongly prefer attachment to the carbon support.

The SEM image in Figure 25 shows that many of the platinum nanostructures grown onto carbon are globular nanodendrites that conform to the shape of the underlying carbon support. An EDX spectrum (Figure 26) shows that the light globular structures are platinum. (The copper peaks arise from the TEM sample grid.)

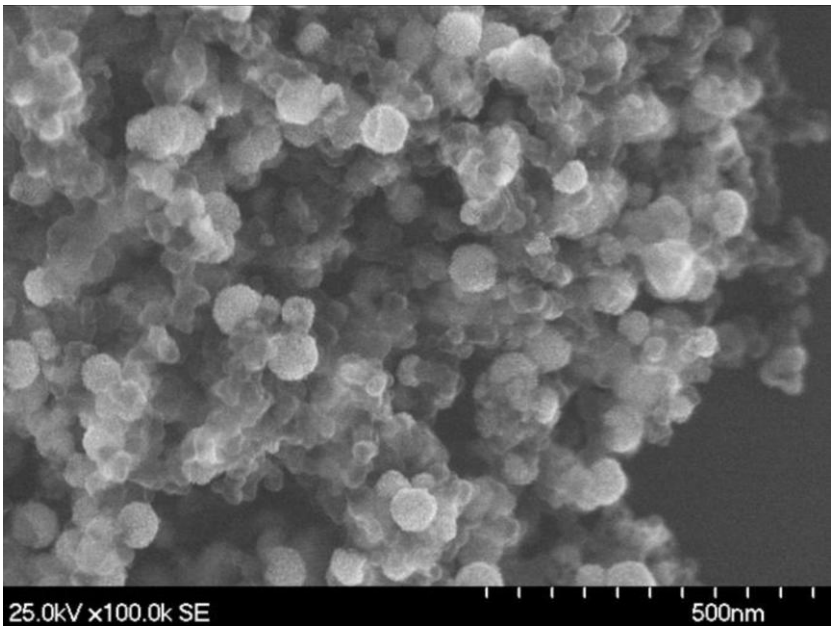

Figure 25. SEM images of platinum nanodendrites supported on CB.

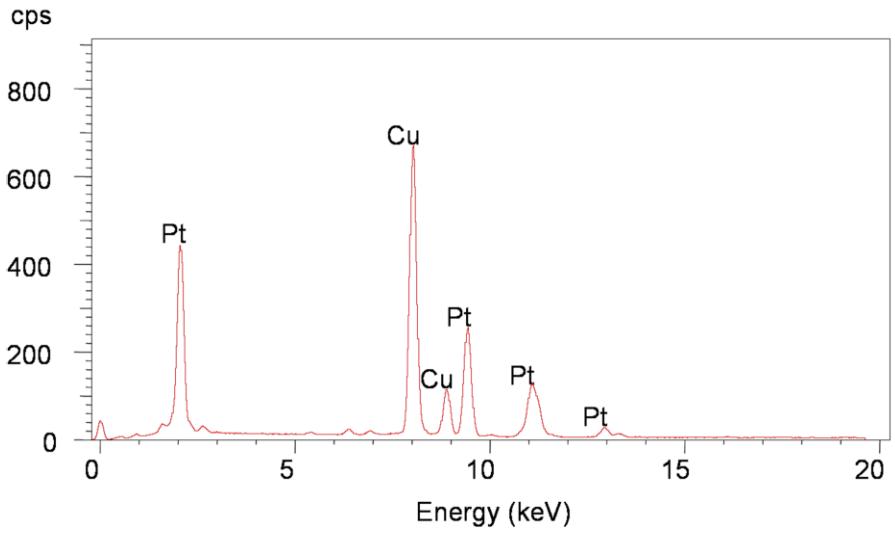

Figure 26. EDX of the platinum dendrites/CB nanocomposites (copper peaks come from the TEM sample grid).

XPS spectroscopy was used to determine the oxidation state of platinum (Figure 27). The Pt (4f) signals of a low energy band (4f7/2) at 71.4 eV, and a high-energy band (4f5/2) centering at 3.2 eV higher reveal that the deposited Pt nanodendrites are in the form of zero-valent metal.

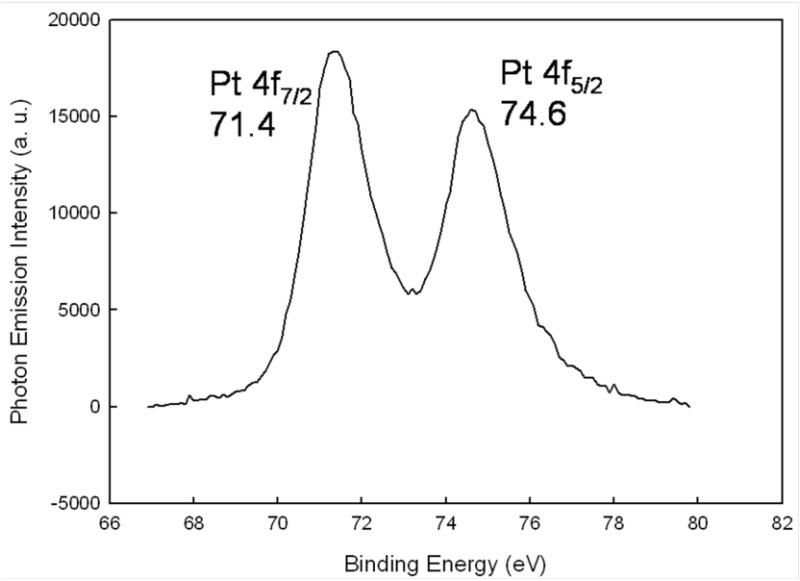

Figure 27. Pt 4f core level XPS spectrum of the nanocomposites.

The XRD pattern of the hemispherical globular platinum dendrites is shown in Figure 28. The peaks match well with that expected for fcc Pt crystals. The three peaks are attributed to 111, 200, and 220 reflections, respectively. The peak broadening is consistent with the nanoscale structural features of the Pt dendrites.

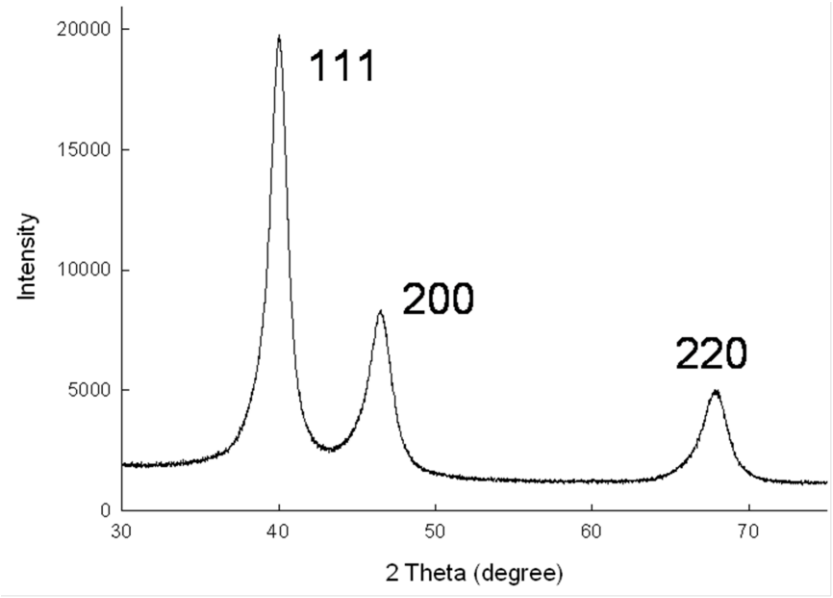

Figure 28. XRD pattern of the nanodendrites supported on CB.

The platinum loading on CB was examined using thermal analysis. In the measurement, the carbon black is oxidized and vaporized, and the weight loss of the material is continuously monitored. Figure 29 shows the sample weight change and the temperature difference between the sample crucible and an empty reference crucible during heating in dry air. There is little weight loss at temperatures below 320 ºC, but a steep drop is observed at higher temperatures. The weight decrease is attributed to complete oxidation and loss of CB. The curve levels out at 540 ºC and the remaining weight is measured to be 42.5% of the original, which is close to the targeted 45% platinum loading. This verifies that the platinum loading can be controlled in this reaction by varying initial concentrations of the Pt precursor.

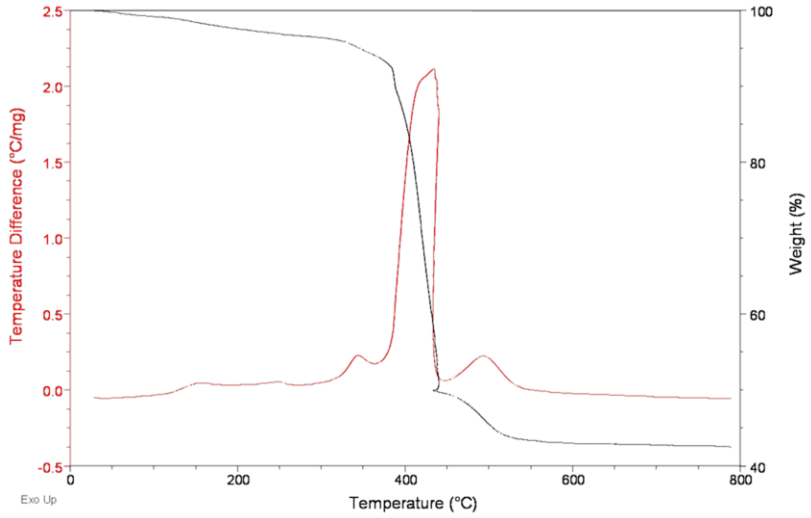

Figure 29. DTA-TGA diagram of the nanocomposites with dried air as flow media.

Accordingly, more syntheses were conducted in the presence of aged aqueous platinum complexes ranging from 10, to 0.64, to 0.28 mM, which are corresponding to 80, 20, and 10 wt% of platinum loading on carbon, respectively. Figure 29 shows that with the reduction of platinum loading on carbon, the average diameter of platinum nanodendrites decreases from 55.9 to 25.9, to 18.6, to 14.5 nm, which are determined by the measurements of 100 randomly selected individual dendrites in each sample (For easy comparison, the 45wt% sample using 2.1 mM of the platinum complexes was also included). However, all of the samples have a relatively large average diameter and a wide size distribution because of a slow and continuous seeding process proposed before to explain the growth of metallic nanoparticles.[39] The ratio between standard deviation and average diameter is calculated to be 26 to 38%. To realize size and size uniformity control over the materials, we aimed to combine a photocatalytic seeding strategy to the synthesis as described in the following.

5.4 Photocatalytic Generation of Platinum Seeds

Traditional particle-seeding is a widely applied method for size and size uniformity control over a series of nanomaterials.[40] Alternatively, our group has developed a tin(IV) porphyrin (SnP) based photocatalytic seeding approach, which is easy, fast, and photo-controllable and can produce a large initial concentration of seeds.[29] However, our previous platinum seeds were prepared in the presence of surfactant assemblies. To keep the reaction system simple, it is necessary to synthesize platinum seeds in the absence of surfactants. In addition, CB absorbs light and can interfere with the photocatalysis process, which requires us to design a multiple-step synthesis to separate the photocatalytic seeds production from the seeds growth step. Firstly, we will focus on the synthesis of well dispersed platinum seeds (nanoparticles).

The rapid generation of seeds by white light irradiation of a tin-porphyrin (SnP) photocatalyst is described by the following simplified equations:

$$SnP + h\nu \rightarrow SnP^*$$
$$SnP^* + ED \rightarrow SnP\text{-}\bullet + EDox$$
$$2SnP\text{-}\bullet + Pt2+ \rightarrow 2SnOEP + Pt0$$

where the photocatalysts in this case are different water soluble SnPs and AA is used as the electron donor (ED). It is known that platinum nanoparticles need to be stabilized by certain species; otherwise they will agglomerate together and cannot well serve the purpose of being used as seeds. So, five water-soluble SnP carrying different functional groups were selected and expected to function as both photocatalysts and stabilizers (Figure 22). In our reaction systems, the pH value is buffered at 3 by 75 mM of AA. Under these solution conditions, SnNMePyP and SnTPPS4 carry positive and negative charges, respectively, and SnProP, SnUroP, and SnTCPP are electronically neutral. The TEM image in Figure 30d shows that only SnTPPS4 led to the formation of fairly dispersed platinum nanoparticles while the other SnPs resulted in agglomerations of particles (Figure 30a,b,c,e).

We speculate that the charges on SnPs play an important role in the syntheses. For the seeding purpose, only the reaction system involving SnTPPS4 is promising. After examining the

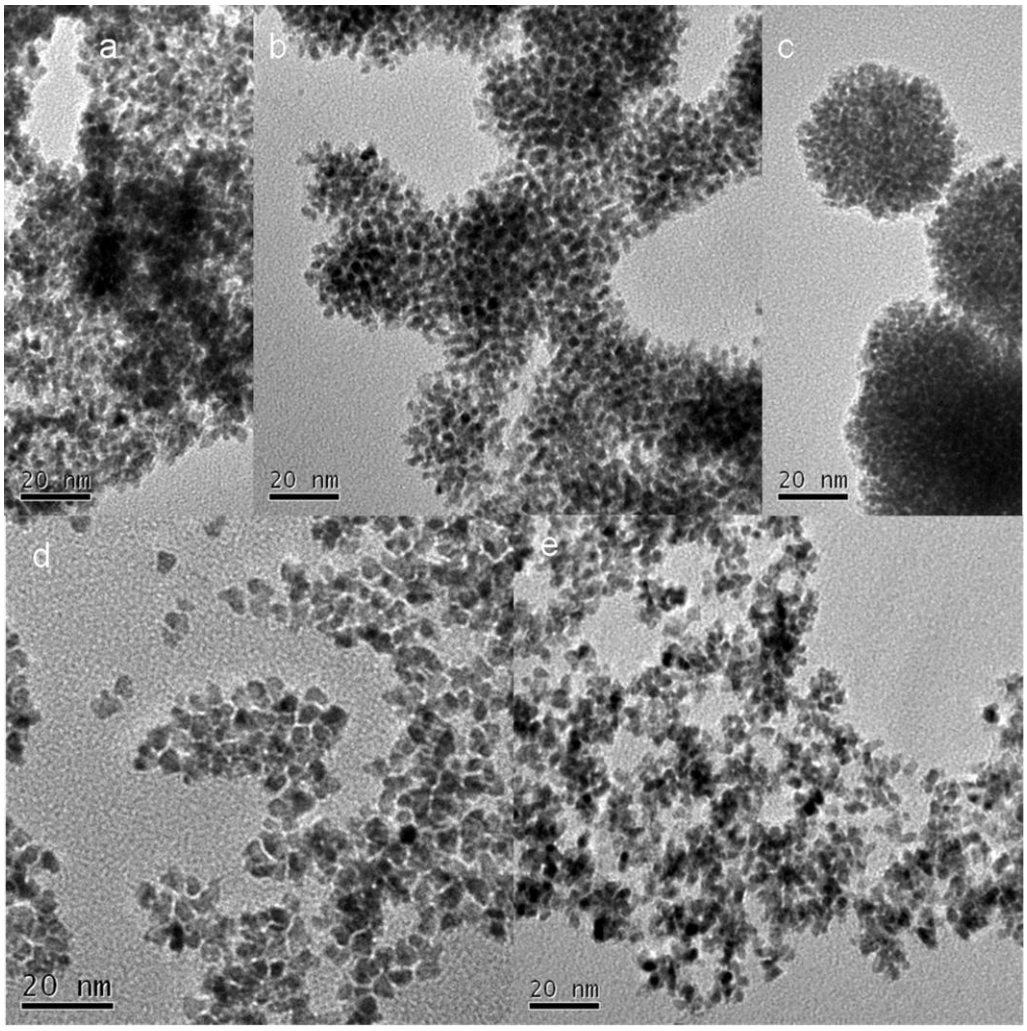

Figure 30. TEM images of platinum nanostructures photocatalytically produced using various concentrations of tin porphyrins: (a) 38 μM SnProtoP, (b) 32 μM SnUroP, (c) 50 μM SnNMePyP, (d) 50 μM SnTPPS4, and (e) 35 μM SnTCPP.

concentration of platinum complexes (0.5-5 mM) and SnTPPS4 (30-250 μM), a reaction system was finally identified to be capable of producing well separated platinum seeds. The reaction system is composed of 1-2 mM Pt(II), 83-150 μM SnTPPS4, and 75 mM AA. At a platinum concentration lower than 1 mM, the number of seeds is relatively low. A concentration of platinum salt higher than 2 mM generally leads to large platinum seeds, some of which show dendritic buds (images not shown). As far as the concentration of SnTPPS4 is concerned, a low concentration of SnTPPS4 such as 50 μM (Figure 30d) results in relatively large platinum nanoparticles with some aggregation because of a low number of photocatalytic reaction centers. In contrast, a concentration of SnTPPS4 higher than 150 μM cannot significantly improve the quality of the seeds in terms of the size and dispersion of particles. This is possibly due to the shielding effect among SnTPPS4 molecules at such a high concentration (image not shown). Figure 31 shows typical TEM images of well separated platinum nanoparticles synthesized by using 1 mM Pt(II) and 83 μM of SnTPPS4. The sizes of the particles ranging from 2 to 6 nm are

still large and define the lower size limit of the seeded sample to be relatively large also. However, to prove the seeding concept these seeds are fairly good.

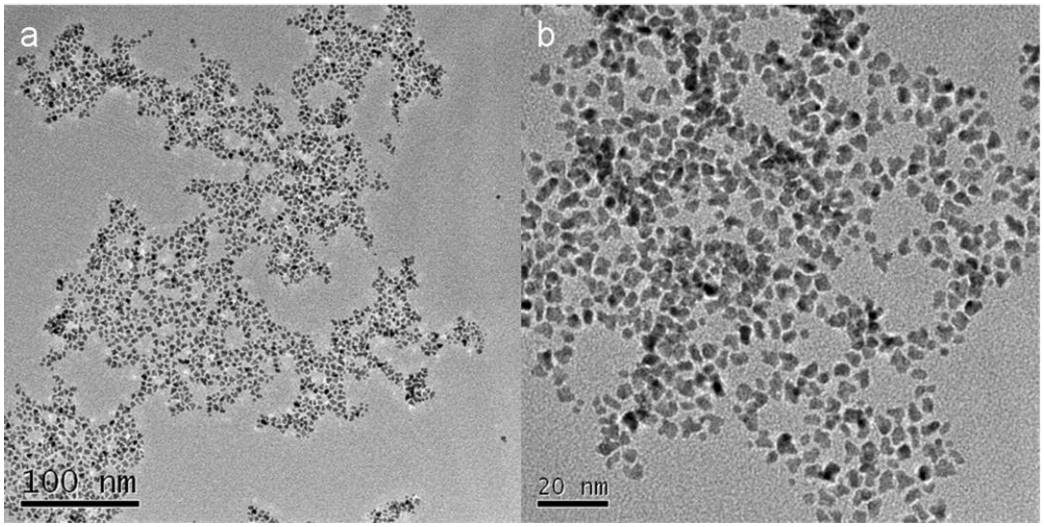

Figure 31. TEM images of platinum seeds at low (a) and high (b) magnifications prepared by using 83 μM of SnTPPS4 and 2 mM of aged aqueous K_2PtCl_4.

5.5 Seeded Growth of Platinum Dendrites on Carbon

The principle of the seeding strategy is to provide nearly equal growth times for each of the nucleation centers, resulting in a uniform size and narrow size distribution. The as-prepared seeds shown in Figure 10 were utilized in the seeded growth of platinum nanodendrites supported on carbon. A simple synthetic procedure is illustrated in Figure 32.

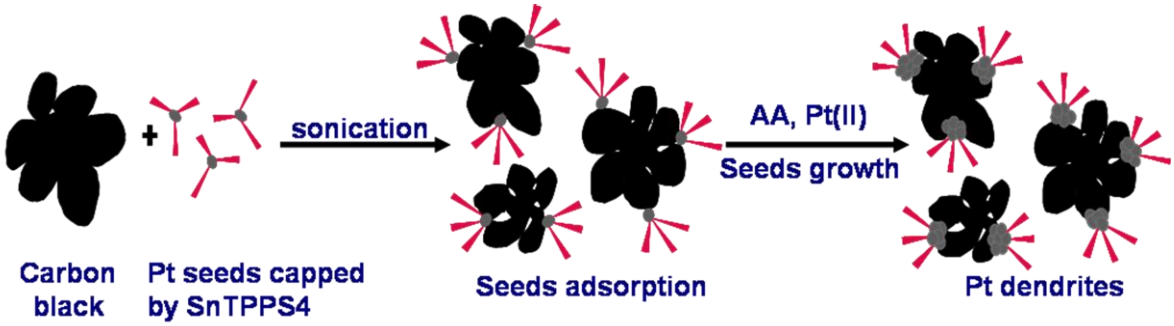

Figure 32. Scheme for the seeded synthesis of uniform platinum nanodendrites on carbon.

Initially, a certain amount of previously generated platinum seeds stabilized by SnTPPS4 molecules were mixed with CB by mild sonication for at least 5 minutes. This is an easy and efficient avenue for seeds adsorption on carbon. When 1 mL of seeds was mixed with 10 mg CB as the above procedure, CB can be readily precipitated out by centrifuge with nearly transparent and colorless supernatant. This verifies that platinum seeds have been physically adsorbed by carbon as expected. The high surface area of carbon black (about 800 m^2/g) may account for the effective adsorption. Subsequently, aged platinum complexes (2.05 mL of 20 mM platinum

complexes) and AA (10 mL of 150 mM AA) were added under stirring to allow autocatalytic growth [41] of the seeds into uniform nanodendrites.

The average size of the dendrites can be controlled by varying the ratio between the number of seeds and the amount of metal complex. For the purpose of identifying the seeding effect, the

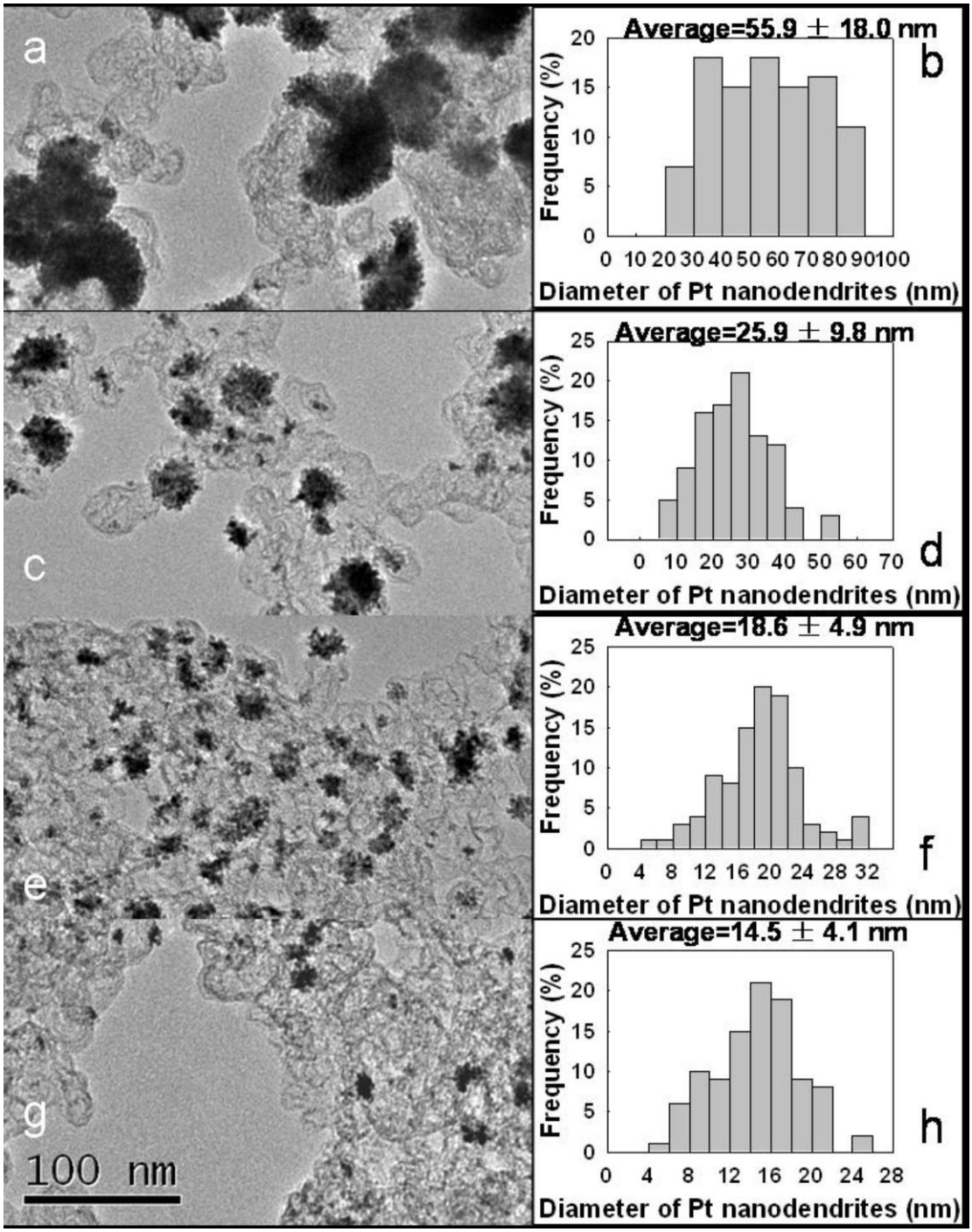

Figure 33. TEM images of dendritic platinum nanostructures supported on CB in the presence of 10 (a), 2.1 (c), 0.64 (e), and 0.28 mM (g) of K_2PtCl_4 aqueous salt and their corresponding size distribution plot (c, d, f, and h) with average size and standard deviation.

total platinum loading on carbon from both the seeds and additional metal source was held at 45wt% in the seeded experiments.

Figures 33 and 34 compare the results of unseeded and seeded growth of Pt dendrites on carbon black. TEM analysis (Figure 34a) reveals that uniform dendrites are obtained. Statistical analysis of 100 randomly selected nanodendrites gives an average diameter of 17.6 ± 4.3 nm (Figure 34b), which is much smaller than that of those attained (25.9 ± 9.8 nm) in the absence of the

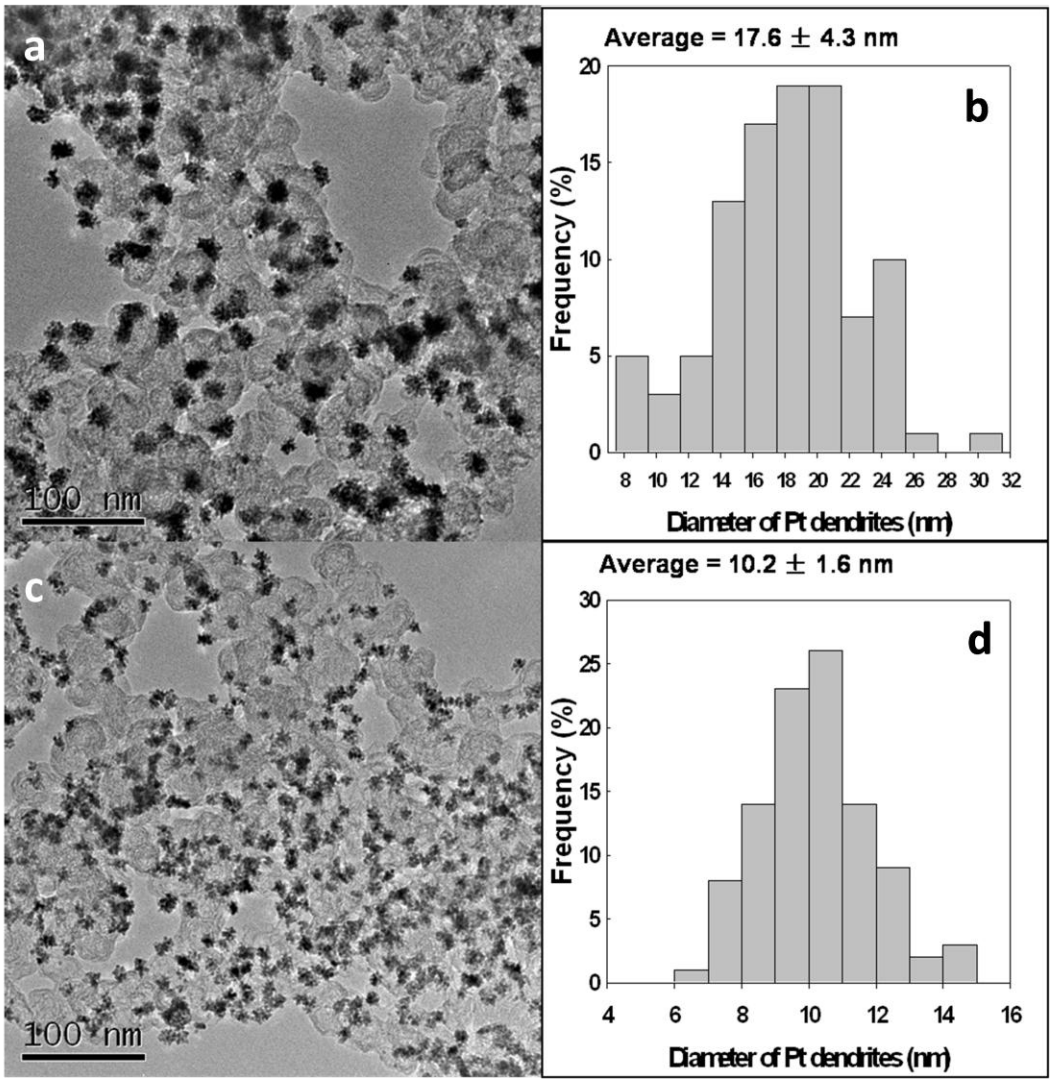

Figure 34. TEM images of seeded platinum nanodendrites on carbon using 1 mL (a) and 5 mL (c) of photocatalytically generated platinum seeds and their corresponding histogram of size distribution (b) and (d).

added seeds (Figure 24a, b and Figure 33c). The apparent reduction of the average size can be attributed to the increased number of seeds, which causes a decreased percentage of platinum distributed to each seed at a constant total platinum source. On the other hand, the ratio (24%) between the standard deviation to the average size does not improve much compared with the

ratio of the sample without seeding (38%). The reason might be the number of seeds used in the reaction is relatively low and cannot compete well with the slow and continuous seeding process. To take into account this competition, 5 mL of the seeds and 10 mg CB were employed. In this case, carbon black cannot be precipitated out by centrifuge after sonication. We propose that the negatively charged SnTPPS4 molecules on platinum seeds have significantly modified the surface of carbon black, making the carbon particles carry negative charges, repel each other and become stable. As shown in Figure 34c, d, the increased number of seeds leads to a further reduced average size with a narrow size distribution (10.2 ± 1.6 nm, 16%) as expected. The 5 mL of seeds can compete well with the slow and continuous seeding process and dominates the growth of dendrites. When 10 mL of seeds per 10 mg carbon is tested, a large number of unsupported and smaller platinum nanodendrites are observed. In this case, it seems that CB cannot provide enough nucleating sites to adsorb all the seeds. In this scenario, when Vulcan-XC 72R CB was used (about 250 m^2/g) [21] in the seeding experiments, more unsupported dendrites are observed. This proves that the high surface area of CB is a key factor for the seeded synthesis.

In conclusion, globular platinum dendrites/CB nanocomposites with controllable metal loadings were synthesized in a gram scale via a simple chemical reduction. The size and size uniformity of the Pt dendrites are easily controlled by the addition of photocatalytically generated, porphyrin-stabilized Pt nanoparticles as seeds. Further improvements in the size and size uniformity can be expected when using smaller seeds, which may be produced with a very intense light exposure and a better stabilizer. The Pt dendrites-CB nanocomposites are potentially useful in catalytic and electrocatalytic applications. This study opens up opportunities of growing shaped and size-controllable platinum nanostructures other than particles on CNMs.

6. Conclusions

Methods for covalently attaching dendritic platinum nanostructures to electrode surfaces have been developed and shown to yield stable, functional electrocatalytic structures. The dual-diazonium method demonstrated is applicable to a wide variety of nanostructure and electrode substrate material types. Electrochemical scanning tunneling microscopy was applied to dendritic platinum nanostructures and confirmed the resistance of this structural form to large-scale electrochemically driven Oswald ripening for extended periods of potential cycling through the surface oxide formation and reduction potential range in an acidic electrolyte. The origins of ripening resistance were explored using Kinetic Monte Carlo computation methods emphasizing the critical role negative radius of curvature plays in creating this resistance. Molecular Dynamics simulations were run to determine how a hole within a platinum sheet, formed from the evolution of the original dendritic form, evolves as a function of thermal energy input. Direct growth of dendritic platinum nanostructures onto graphitic carbon particles was explored. A two-step photocatalytic seeding process was developed in which the resulting dendritic nanostructure size can be controlled. This latter discovery could be exploited to produce strongly anchored, ultra-low loadings of platinum for reversible oxygen electrochemistry in fuel cell and air battery applications.

7. References

1. Rolison, D.R., *Science*, **2003**, 299, 1698.
2. Song, Y.; Hickner, M. A.; Challa, S. R.; Dorin, R. M.; Garcia, R. M.; Wang, H.; Jiang, Y.-B.; Li, P.; Qiu, Y.; van Swol, F.; Medforth, C. J.; Miller, J. E.; Nwoga, T.; Kawahara, K.; Li, W.; Shelnutt, J. A. Nano Lett. 2009, 9, 1534.
3. Bi, W., Fuller, T.F. J. Power Sources, 2008, 178, 188.
4. Virkar, A.V. and Zhou, Y., *J. Electrochem. Soc.*, **2007**, 154, B540.
5. Colon-Mercado, H.R. and Popov, B.N., J. Power Sources, **2006**, 155, 253.
6. S. Mahouche-Chergui, S. Gam-Derouich, C. Mangeney, and M. M. Chehimi, Chem. Soc. Rev., 2011, 40, 4143.
7. A. Adenier, E. Cabet-Deliry, A. Chausse, S. Griveau, F. Mercier, J. Pinson, and C. Vautrin-Ul, Chem. Mater., **2005**, 17, 491.
8. Kariuki, J. K. and McDermott, M. T., *Langmuir*, **1999**, 15, 6534.
9. Stöhr, J., *NEXAFS Spectroscopy*, Springer-Verlag, Berlin, 1996.
10. Kong, J.; Chapline, M. G.; Dai, H. J. *Adv. Mater.* **2001**, *13*, 1384.
11. Yang, M. H.; Yang, Y. H.; Liu, Y. L.; Shen, G. L.; Yu, R. Q. *Biosensors & Bioelectronics* **2006**, *21*, 1125.
12. Qu, F. L.; Yang, M. H.; Shen, G. L.; Yu, R. Q. *Biosensors & Bioelectronics* **2007**, *22*, 1749.
13. Hrapovic, S.; Liu, Y. L.; Male, K. B.; Luong, J. H. T. *Anal. Chem.* **2004**, *76*, 1083.
14. Kim, H. S.; Lee, H.; Han, K. S.; Kim, J. H.; Song, M. S.; Park, M. S.; Lee, J. Y.; Kang, J. K. *J. Phys. Chem. B* **2005**, *109*, 8983.
15. Yoo, E.; Gao, L.; Komatsu, T.; Yagai, N.; Arai, K.; Yamazaki, T.; Matsuishi, K.; Matsumoto, T.; Nakamura, J. *J. Phys. Chem. B* **2004**, *108*, 18903.
16. Sheeney-Haj-Ichia, L.; Basnar, B.; Willner, I. *Angew. Chem. Int. Ed.* **2005**, *44*, 78.
17. Vielstich, W.; Lamm, A.; Gasterger, H. A. *Handbook of Fuel Cells Fundamentals, Technology and Applications*; John Wiley & Sons: New York, 2003.
18. Vijayakrishnan, V.; Santra, A. K.; Seshadri, R.; Nagarajan, R.; Pradeep, T.; Rao, C. N. R. *Surf. Sci.* **1992**, *262*, L87.
19. Planeix, J. M.; Coustel, N.; Coq, B.; Brotons, V.; Kumbhar, P. S.; Dutartre, R.; Geneste, P.; Bernier, P.; Ajayan, P. M. *J. Am. Chem. Soc.* **1994**, *116*, 7935.
20. Hsin, Y. L.; Hwang, K. C.; Yeh, C. T. *J. Am. Chem. Soc.* **2007**, *129*, 9999.
21. Georgakilas, V.; Gournis, D.; Tzitzios, V.; Pasquato, L.; Guldi, D. M.; Prato, M. *J. Mater. Chem.* **2007**, *17*, 2679.
22. Narayanan, R.; El-Sayed, M. A. *Nano Letters* **2004**, *4*, 1343.
23. Narayanan, R.; El-Sayed, M. A. *J. Phys. Chem. B* **2004**, *108*, 5726.
24. Narayanan, R.; El-Sayed, M. A. *J. Am. Chem. Soc.* **2004**, *126*, 7194.
25. Narayanan, R.; El-Sayed, M. A. *Langmuir* **2005**, *21*, 2027.
26. Song, Y. J.; Challa, S. R.; Medforth, C. J.; Qiu, Y.; Watt, R. K.; Pena, D.; Miller, J. E.; van Swol, F.; Shelnutt, J. A. *Chem. Comm.* **2004**, 1044.
27. Song, Y. J.; Jiang, Y. B.; Wang, H. R.; Pena, D. A.; Qiu, Y.; Miller, J. E.; Shelnutt, J. A. *Nanotechnology* **2006**, *17*, 1300.
28. Song, Y. J.; Yang, Y.; Medforth, C. J.; Pereira, E.; Singh, A. K.; Xu, H. F.; Jiang, Y. B.; Brinker, C. J.; van Swol, F.; Shelnutt, J. A. *J. Am. Chem. Soc.* **2004**, *126*, 635.

29. Song, Y.; Dorin, R. M.; Garcia, R. M.; Jiang, Y.-B.; Wang, H.; Li, P.; Qiu, Y.; van Swol, F.; Miller, J. E.; Shelnutt, J. A. *J. Am. Chem. Soc.* **2008**, *130*, 12602.
30. Song, Y. J.; Steen, W. A.; Pena, D.; Jiang, Y. B.; Medforth, C. J.; Huo, Q. S.; Pincus, J. L.; Qiu, Y.; Sasaki, D. Y.; Miller, J. E.; Shelnuttt, J. A. *Chem. Mater.* **2006**, *18*, 2335.
31. Song, Y. J.; Garcia, R. M.; Dorin, R. M.; Wang, H. R.; Qiu, Y.; Shelnutt, J. A. *Angew. Chem. Int. Ed.* **2006**, *45*, 8126.
32. Song, Y. J.; Garcia, R. M.; Dorin, R. M.; Wang, H. R.; Qiu, Y.; Coker, E. N.; Steen, W. A.; Miller, J. E.; Shelnutt, J. A. *Nano Lett* **2007**, *7*, 3650.
33. Ciacchi, L. C.; Pompe, W.; De Vita, A. *J. Am. Chem. Soc.* **2001**, *123*, 7371.
34. Song, Y.; Hickner, M. A.; Challa, S. R.; Dorin, R. M.; Garcia, R. M.; Wang, H.; Jiang, Y.-B.; Li, P.; Qiu, Y.; van Swol, F.; Medforth, C. J.; Miller, J. E.; Nwoga, T.; Kawahara, K.; Li, W.; Shelnutt, J. A. *Nano Lett.* **2009**, *9*, 1534.
35. Garcia, R. M.; Song, Y.; Dorin, R. M.; Wang, H.; Li, P.; Qiu, Y.; van Swol, F.; Shelnutt, J. A. *Chem. Commun.* **2008**, 2535.
36. Wang, H.; Wang, Z.; Medforth, C. J.; Miller, J. E.; Evans, L.; Li, P.; Shelnutt, J. A. *Chem. Mater.* **2008**, *20*, 7434.
37. Wang, Z. L. *Adv. Mater.* **2003**, *13*, 1497.
38. Watzky, M. A.; Finke, R. G. *J. Am. Chem. Soc.* **1997**, *119*, 10382.
39. Jana, N. R.; Gearheart, L.; Murphy, C. J. *Langmuir* **2001**, *17*, 6782.
40. Greenbaum, E. *J. Phys. Chem.* **1988**, *92*, 4571.

DISTRIBUTION

5	MS0888	K.R. Zavadil	1825
1	MS1411	F.B. van Swol	1814
1	MS1415	N.A. Missert	1112
1	MS 0889	S.J. Glass	1825
1	MS 0899	RIM- Reports Management	9532 (electronic copy)
1	MS0359	D. Chavez, LDRD Office	1911


Sandia National Laboratories